Full length article

A tribocorrosion appraisal of a dual layer PVD coated CoCrMo alloy tribopair

Antonino Mazzonello [a], Joseph Buhagiar [a], Raisa Chetcuti [a], Peter A. Dearnley [b], Andrea Valsesia [c], Pascal Colpo [c], Bertram Mallia [a,*]

[a] Department of Metallurgy and Materials Engineering, University of Malta, Msida, MSD 2080, Malta
[b] Boride Services Ltd, Blakedown DY10 3NE, United Kingdom
[c] European Commission, Joint Research Center (JRC), Ispra, Italy

ARTICLE INFO

ABSTRACT

A dual layer PVD coating consisting of a CrN layer on top of a CoCrMo(C) S-phase underlayer (CrN/S) was deposited on low-carbon wrought CoCrMo alloy discs and CoCrMo Stellite® 21 spheres. The tribocorrosion response of the uncoated CoCrMo tribopairs and coated CrN/S tribopairs was studied under reciprocating sliding conditions in Ringer's and diluted foetal bovine serum (FBS) solutions under anodic potential and elastic contact for a sliding time of 2 h. Compared to the uncoated tribopair, CrN/S successfully mitigated both oxidation and mechanical material losses and resulted in a low dynamic coefficient of friction and smoother scar morphologies in both test solutions. For the uncoated tribopair, the presence of proteins acted as a barrier to charge transfer and lowered the friction during tribocorrosion testing contributing to a marked reduction in material loss, primarily by a reduction in oxidative losses, but resulted in a rougher scar morphology. Tribocorrosion tests of the coated tribopair were also carried out for a duration of 24 h and revealed minimal material losses in diluted FBS and no evidence of other damage. It, however, resulted in substantial thinning of the outer CrN layer, transverse microcracking and delamination when testing in Ringer's solution. This coating loss produced a source for coating debris which led to three-body micro-abrasion damage. FIB investigation revealed that the observed transverse microcracks were limited to the outer layer and hence have not provided electrolytic pathways to the substrate interface. The excellent tribocorrosion response of dual layer CrN/S on CoCrMo metal tribopairs in diluted FBS renders them good candidates for further investigation to mitigate tribocorrosion damage of biomedical CoCrMo alloys.

1. Introduction

A typical environment in the human body where tribocorrosion (or corrosion-wear) related mechanisms prevail is in the articulating components of the hip joint. These components are subjected to the combined effect of mechanical wear and chemical attack governed by body fluids. CoCrMo alloys have been the materials of choice for load bearing surfaces including orthopaedic implants for over six decades, owing to their optimal mechanical properties and good corrosion resistance [1,2]. However, serious concerns started to arise on the use of metallic alloys in the biomedical field following a study on data obtained from the National Joint Registry of England and Wales for primary total hip arthroplasties (THAs) between 2003 and 2011 published in The Lancet [3]. The study did not recommend the use of metal-on-metal (MoM) implants for use as articulating surfaces due to their low survival rate. Other authors [4–7] highlighted several deficiencies related with the clinical impact of tribocorrosion processes on MoM implants, such as aseptic loosening, peri-prosthetic bone resorption, adverse biological reactions induced by corrosion products, and the release of high Cr and Co ions levels.

A final order [8] by the Food and Drug Administration (FDA), which became effective from May 2016, made it a requirement for manufacturers of MoM implants to file a premarket approval. This is the most stringent regulatory category of the FDA's oversight for medical devices. To market such devices, it is now a requirement by all manufacturers of MoM total hip implants to submit premarket approvals. As it stands, there are currently no FDA-approved MoM total hip joint replacement devices which are marketed for use in the USA but there are two FDA-

Table 1

Chemical composition of the ASTM F1537-20 CoCrMo alloy substrate (supplied by L. Klein) and Stellite® 21 CoCrMo spherical balls (supplied by Kennametal Stellite GmbH).

	Chemical composition of Biodur® CCM CoCrMo alloy (wt%)										
	C	Mn	Si	Cr	Ni	Mo	Fe	W	N	Cu	Co
Biodur® CCM alloy	0.05	0.80	0.62	27.64	0.07	5.46	0.20	0.02	0.17	0.01	Bal.
Stellite®21 alloy	0.23	0.45	1.50	26.80	2.80	5.50	0.80	0.13	/	/	Bal.

approved MoM hip resurfacing devices available on the market. These two devices are the Cormet Hip Resurfacing System (Corin USA Ltd.) and the Birmingham Hip Resurfacing (BHR) System (Smith & Nephew Inc.). As a result to this final order published by the FDA, the popularity of MoM implants decreased significantly [9].

Notwithstanding the above, there are still many advantages offered by MoM implants. In fact, this material combination is still used in hip-resurfacing systems which offer the ability to preserve bone stock, especially in young patients [6,10]. In addition, the use of MoM implants ensures a better fracture resistance than typical ceramic-on-ceramic implants [10,11]. In view of the issues associated with MoM implants, the scope of this study is to find solutions to mitigate such shortcomings.

Physical vapour deposition (PVD) is a technique that has been used to deposit thin coatings on biomedical alloys to improve their tribological response [12]. PVD coatings can be manipulated to meet specific requirements of biomaterials proposed for bearing surfaces of orthopaedic implants such as wear resistance [13], low friction [14], chemical inertness [15] and biocompatibility [16]. Magnetron sputtering is a versatile PVD technology which utilises a confined gaseous plasma to enable erosion of target material via bombardment of high energy ions in an inert or reactive reduced pressure environment enabling the deposition of thin coatings. Such technology has been used to deposit ceramic and S-phase coatings on biomedical alloys [12,17]. S-phase is a metastable, precipitate free, interstitial supersaturated and a hard "expanded austenite" with a face centred cubic (FCC) crystal structure [18]. S-phase coating is produced via magnetron sputtering of austenitic stainless steel or CoCrMo alloys in the presence of nitrogen or carbon containing atmosphere [12,17]. Such coatings result in high hardness (>12 GPa), good corrosion resistance and excellent load-bearing capabilities. The deposition of PVD sputtered CoCrMo(C) S-phase is a recently implemented concept in biomedical implants since previous work [19–21] was mainly focused on the S-phase being produced on metallic alloys via low temperature diffusion treatments. Previous work [17] has shown that CoCrMo(C) coatings were successful in retaining an excellent corrosion resistance when exposed to Ringer's solution. Similarly, S-phase coatings decreased the tribocorrosion damage on stainless steel but were not as effective as CrN coatings [17,22].

The applicability of monolayered PVD CrN coatings has been extensively scrutinised by many researchers but knowledge on the design of multi-layered PVD coatings is still underexplored [17]. Previous studies [12] showed that CrN coatings deposited on CoCrMo suppressed oxidation losses (also referred to as Type I corrosion-wear). An earlier study [17] conducted by the authors has also shown that the interface between the CrN and CoCrMo(C) coating layers was resistant to catastrophic-type failure (also referred to as Type II corrosion-wear) with the CoCrMo(C) coating layer being also able to provide sufficient load bearing support such that coating integrity was maintained. The high hardness and inherent chemical inertness of CrN coatings make them good candidates to limit debris and ion release, as shown in previous studies [23,24] using a hip simulator. Leslie et al. [23] reported reduced wear for CrN-coated implants compared to uncoated MoM controls under standard walking conditions with correctly aligned and concentric components. However, in a later study [24], the same authors investigated scenarios which depart from perfect alignment of the bearings, whereby the bearing surfaces were exposed to regions of higher stresses. Under such adverse conditions, the wear rate of the uncoated MoM tribopairs resulted to be much higher (by 17-fold)

then when tested under standard walking conditions [24]. In the same study [24], two of the CrN-coated implants exhibited stripe wear and rim wear on the cup such that the coated tribopairs produced increased wear compared to uncoated MoM. The failure observed in [24] could be attributed to inadequate load support of the hard CrN coating. A strategically designed dual layer coating can be the solution to mitigate the formation of paths for the electrolyte to reach the substrate-coating interface, ultimately suppressing Type II corrosion-wear.

Indeed, a recent publication by Chetcuti et al. [17] has shown that the material losses of 316LVM stainless steel were successfully mitigated via the application of a dual-layered coating system when sliding against an alumina counterface in Ringer's solution. Similarly, Sun et al. [12] have shown promising results on the application of a CrN layer on top of a CoCrMo(C) S-phase layer deposited on an ASTM F75-18 CoCrMo substrate. This dual layer coating system displayed reduced oxidation losses and excellent resistance to catastrophic coating failure when rubbed against an alumina counterface in a unidirectional sliding motion in a saline solution. Therefore, such published works [12,17] show the potential and beneficial effect of having a dual-layered coating when compared to monolayer coatings.

This work shall focus on a dual layer coating consisting of a top CrN layer and a CoCrMo(C) S-phase layer underneath deposited using magnetron sputtering on a medical grade ASTM F1537-20 CoCrMo substrate (denoted as CrN/S). A novel approach to the work carried out by Sun et al. [12] is proposed in this work whereby a PVD coated CoCrMo alloy counterface will be used in tribocorrosion experiments. While the use of an inert counterface (such as α-Al$_2$O$_3$) simplifies the electrochemical measurements, the approach adopted in this work replicates better the MoM implant conditions. The influence of proteins on the tribocorrosion behaviour of the uncoated CoCrMo alloy and the dual layer coated MoM tribopairs is studied by testing in both a saline and a protein-rich solution.

2. Materials and methods

2.1. Substrate materials

The disc substrates were cut from a low-carbon wrought Biodur® CCM CoCrMo alloy (L. Klein, Switzerland) produced by vacuum induction melting followed by electroslag remelting. The composition of the alloy is given in Table 1 and is conformant with the ASTM HYPERLINK "http://www.astm.org/Standards/F1537"F1537-20 standard – *Standard Specification for Wrought Cobalt-28Chromium-6Molybdenum Alloys for Surgical Implants*. The microstructure of the wrought substrate is composed of equiaxed grains having an average grain size of ~4 μm.
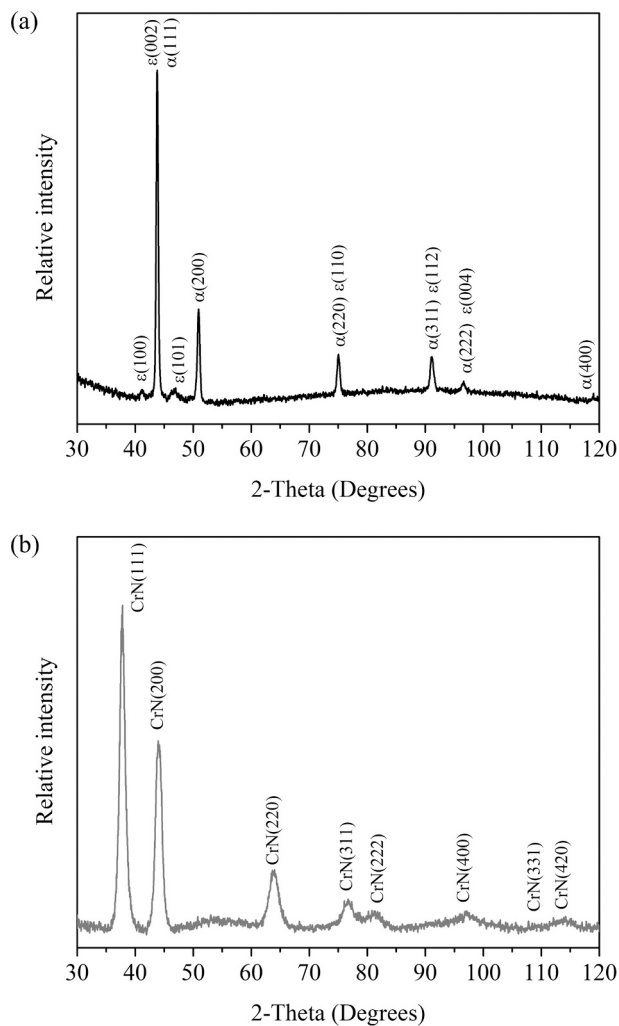
The CoCrMo alloy substrate was supplied as a warm-worked rolled bar and was cut down to flat cylindrical discs having a diameter of 25.4 mm and a thickness of 6.0 mm. The cylindrical discs were then ground using SiC emery papers of grit size of P800, P1200 and P2500 μm (Struers, Denmark). Polishing was then carried out on a Struers Tegramin-25 semi-automatic polisher (Struers, Denmark) using MD-Plus and subsequently MD-Chem polishing cloths to achieve a mirror finish. Prior to each grinding and polishing stage, the discs were ultrasonically cleaned in isopropyl alcohol (IPA) for 15 min and left to dry.

The counterface material used for reciprocating tribocorrosion experiments was a Stellite® 21 CoCrMo alloy (Kennametal Stellite GmbH, Germany) in the form of spherical balls, with a diameter of 12.7 ± 0.1

Table 2

Deposition parameters applied during the PVD process on CoCrMo discs and Stellite® 21 CoCrMo spherical balls at an induced substrate bias voltage of −50 V and a target current of 0.5 A. The substrates were made to rotate at a speed of 4 RPM.

Deposition run	Coating deposition parameters						
	Target material	Chamber pressure (Pa)	Chamber atmosphere	Gas flow (SCCM)	Duration (h)	Interlayer	Functional coating
Part 1: CoCrMo(C) S-phase	Cr	0.25	Argon	3	0.5	Cr	
	CoCrMo	0.15	Argon + CH$_4$	Ar = 3 CH$_4$ = 2	2.5		CoCrMo(C)
Part 2: CrN	Cr	0.29	Argon	3	0.5	Cr	
	Cr	0.29	Argon + N$_2$	Ar = 5 N$_2$ = 3	4.5		CrN

Fig. 1. (a) Bragg-Brentano XRD pattern for uncoated CoCrMo and (b) Glancing angle XRD pattern for CrN/S. X-ray source: Cu K(α) radiation.

microconstituents, one with a high Mo and high Si content and the other having a high Cr content compared to that of the crystallites. EDX mapping revealed a higher carbon concentration in the continuous phase to that of the crystallites. Micropores, with an average size of ~20 μm, were also observed within the continuous phase.

2.2. Coating preparation

A dual layer coating was deposited on CoCrMo disc and Stellite® 21 spherical ball substrates via close field unbalanced magnetron sputtering physical vapour deposition using a custom-built deposition chamber at Boride Services Ltd. (UK). The deposition conditions are summarised in Table 2. Cr and CoCrMo (64 wt% Co, 30 wt% Cr, 6 wt% Mo) target materials with a diameter of 100 mm supplied by Testbourne Ltd. (UK), both having a purity of 99.9% were used. The two magnetron sources were configured to be opposite each other with the rotating sample holder located in the space between them. Prior to deposition, radio frequency sputter cleaning process of the discs and balls was carried out in an argon atmosphere at a pressure of 0.12 Pa with an induced bias voltage of −400 V for an hour to remove any surface contaminants. An induced bias of −50 V and a target current of 0.5 A were then applied on both CoCrMo and Cr targets during the deposition process. A thin adhesion layer of chromium was then deposited on top of the CoCrMo substrate, followed by a CoCrMo(C) S-phase layer. Another thin chromium layer was deposited on the CoCrMo(C) layer followed by a topmost CrN layer. The Cr interlayers were deposited to enhance the adhesion between the CoCrMo(C) S-phase coating to the substrate and between the outer CrN layer and inner CoCrMo(C) S-phase layer. This coating is denoted as CrN/S.

2.3. Chemical composition and material characterisation

The crystalline phase of the uncoated CoCrMo discs was determined using a Bruker D8 X-ray diffractometer (Bruker, USA) in a Bragg-Brentano setup. The crystal structure of the CrN/S coated discs was analysed using a Rigaku Ultima IV X-ray diffractometer (Rigaku, Japan) operated in glancing incidence angle asymmetric bragg (GIAB) configuration. X-rays were directed at an angle of incidence of 3° relative to the surface of the disc using a voltage of 40 kV and a current of 40 mA. The morphology and topography of the CrN/S coated discs were characterised using a Merlin Gemini II field emission gun scanning electron microscope, FEG-SEM, (Carl Zeiss, Germany) equipped with an Apollo X Ametek energy dispersive spectroscope (Ametek, USA) and a Nikon Optiphot-100 light optical microscope (Nikon, Japan) equipped with a Leica DFC290 digital camera (Leica Microsystems, Germany). The

mm. Its chemical composition is given in Table 1. The microstructure of this alloy consisted of crystallites of size ~90 μm which contained dispersed submicron porosity. The boundaries between these crystallites were separated by a continuous phase which contained two

Table 3

Chemical composition of CrN/S coated CoCrMo as determined by area EDS at the coating cross-section. Three repeated readings were taken on each layer.

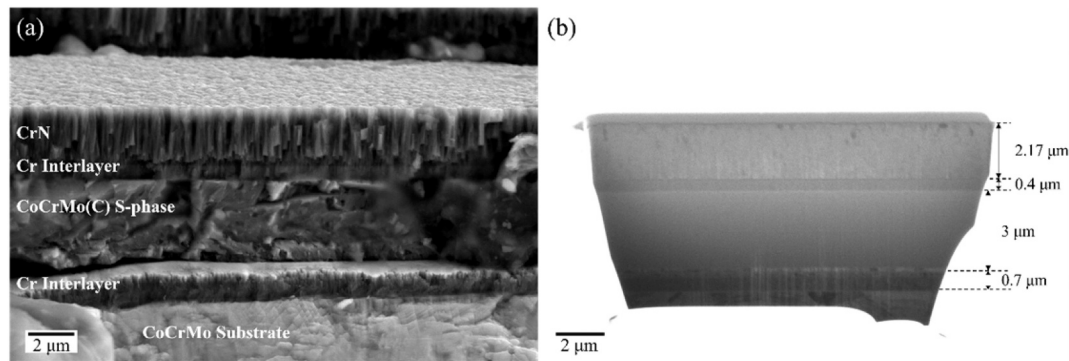| Chemical composition of CrN/S (at.%)							
Position	Layer	Cr	Co	Mo	N	C	O
Top layer	CrN	38.9–39.5	–	–	48.4–50.0	4.7–5.5	5.9–6.8
Bottom layer	S-phase	20.9–25.5	36.0–43.0	2.3–2.7	–	28.0–35.8	1.8–3.8

Fig. 2. (a) A secondary electron SEM image showing the morphology of the fractured disc cross-section of the CrN/S coating deposited on discs, and (b) a focused gallium ion beam image of a CrN/S cross-section showing all the coating layers and their respective thicknesses.

Table 4
Coating thickness and surface roughness on uncoated CoCrMo and CrN/S discs and counterfaces. Error bars represent the average error from the mean.

	Material	Coating thickness (μm)		Surface roughness (nm)	
				R_a	R_q
DISC	CoCrMo	–		7 ± 5	9 ± 6
	CrN/S	CrN	2.6 ± 0.2	42 ± 15	53 ± 13
		S-phase	3.7 ± 0.1		
BALL	CoCrMo	–		126 ± 46	154 ± 54
	CrN/S	CrN	2.4 ± 0.1	167 ± 44	221 ± 56
		S-phase	3.4 ± 0.2		

roughness, R_a and R_q, of the uncoated and CrN/S coated discs and counterfaces was determined using a NanoMap-500LS profilometer (AEP Technology, USA) equipped with a stylus having a tip radius of 1 μm. A scan distance of 800 μm, a scan speed of 25 μms^{-1} (or 10 μms^{-1} for the counterfaces), a contact load of 25 mg and a sample frequency of 50 Hz were used. The spherical profiles of the counterfaces were first levelled using a second-order polynomial and then the surface roughness was measured.

The cross-sectional morphology and thickness of the CrN/S coating on the discs was determined from a fractured cross section. A slit with a depth of ~5.5 mm was cut across the thickness of the disc. The disc was then fractured to reveal the coating cross section. A metallographic cross-section of the coated ball was also prepared so the coating thickness could be measured.

A FEI Nova600 Dual Beam incorporating a gallium focused ion beam (FIB) operated at an accelerating voltage of 30 kV and an ion current of 6.5 nA was used to prepare CrN/S coating cross-sections after depositing a protective platinum stripe. The cross-sectional surface was polished in two steps using an ion current of 93 pA followed by a current of 48 pA. FIB cross-sections complemented microstructural information obtained from the abovementioned fractured cross-sections.

2.4. Mechanical properties

The nano-hardness of the CrN/S coated discs and the ball and disc materials was determined using a Nanomaterials NanoTest 600 machine (Micromaterials, UK) equipped with a Berkovich indenter (nominal radius of 150 nm) at room temperature. Nanoindentation tests were carried out to determine the nano-hardness of the outer CrN layer on the coated discs. Preliminary load-controlled tests were conducted to determine the maximum indentation load which would not result in a penetration depth greater than 10% of the outer CrN layer thickness. The maximum load was determined to be 30 mN. A loading and unloading rate of 0.5 mNs^{-1} at a temperature of 24 °C were used. Nano-hardness measurements, using the same parameters, were carried out on a mirror polished uncoated disc surface and ball cross-section. The

average nano-hardness and standard deviation were determined from 30 repeats carried out on each of the test materials.

A 60° conical diamond indenter of 10 μm radius (Synton Mdp AG, Switzerland) was installed in the Nanomaterials NanoTest 600 machine (Micromaterials, UK) to assess the deformation behaviour of the uncoated CoCrMo disc and coated CrN/S disc samples through nano-scratch tests at room temperature. A constant load of 0.8 mN was first applied for the initial topographical scan, followed by a ramped scratch scan. During this scan, a constant load of 0.8 mN was applied for the first 50 μm of the scratch followed by a gradual increase in load at a rate of 3 mNs^{-1} until a maximum load of 450 mN was reached. A final topographical scan was then performed to determine the surface damage and degree of plastic deformation within the scratch. Each test was repeated five times.

2.5. Test electrolytes

2.5.1. Ringer's solution

Tribocorrosion tests were conducted in Ringer's solution. Eight tablets (Oxoid, UK) were dissolved in 1 L of deionised water to obtain a Ringer's solution (9 g·L^{-1} NaCl, 0.42 g·L^{-1} KCl, 0.48 g·L^{-1} CaCl$_2$ and 0.2 g·L^{-1} NaHCO$_3$) with a pH of 7.4. The isotonic solution of the electrolyte represents the salinity level found in the human body.

2.5.2. Foetal bovine serum

Tribocorrosion tests were conducted in diluted foetal bovine serum (FBS) to investigate the effect of proteins and better mimic the synovial fluid which lubricates the ball and socket joint of a hip during articulation. FBS was supplied (Seralab Ltd., UK) in 500 mL bottles produced from the same batch (0.778 mmol·L^{-1} Calcium, 100 mmol·L^{-1} Chloride, 0.001 mmol·L^{-1} Iron, 0.488 mmol·L^{-1} Phosphorus, 11.7 mmol·L^{-1} Potassium, 140 mmol·L^{-1} Sodium, 16.8 g·L^{-1} albumin, 10.5 g·L^{-1} alpha globulins, 9.0 g·L^{-1} beta globulins and 0.5 g·L^{-1} gamma globulins). FBS was stored at a temperature of −20 °C or lower and was left to completely defrost for 48 h at 4–5 °C prior to use. When FBS was thawed, 0.2 g·L^{-1} of sodium azide (Biochem Chemopharma, France) was added to FBS to preserve the protein fraction. Finally, FBS was diluted using Ringer's solution (preserving the salt content) to achieve a protein concentration of 15.5 g·L^{-1}. This protein concentration selected in this work lies in the lower end of a healthy joint which has been reported to range between 15 and 25 g·L^{-1} [25].

2.6. Tribocorrosion testing

Tribocorrosion experiments were carried out on a custom-built tribocorrosion tester (University of Malta, Malta) in conformance with standard ASTM G133-05 (2016) – *Standard Test Method for Linearly Reciprocating Ball-on-Flat Sliding Wear*. Details of the apparatus used have been provided elsewhere [26]. The tribocorrosion tester was equipped
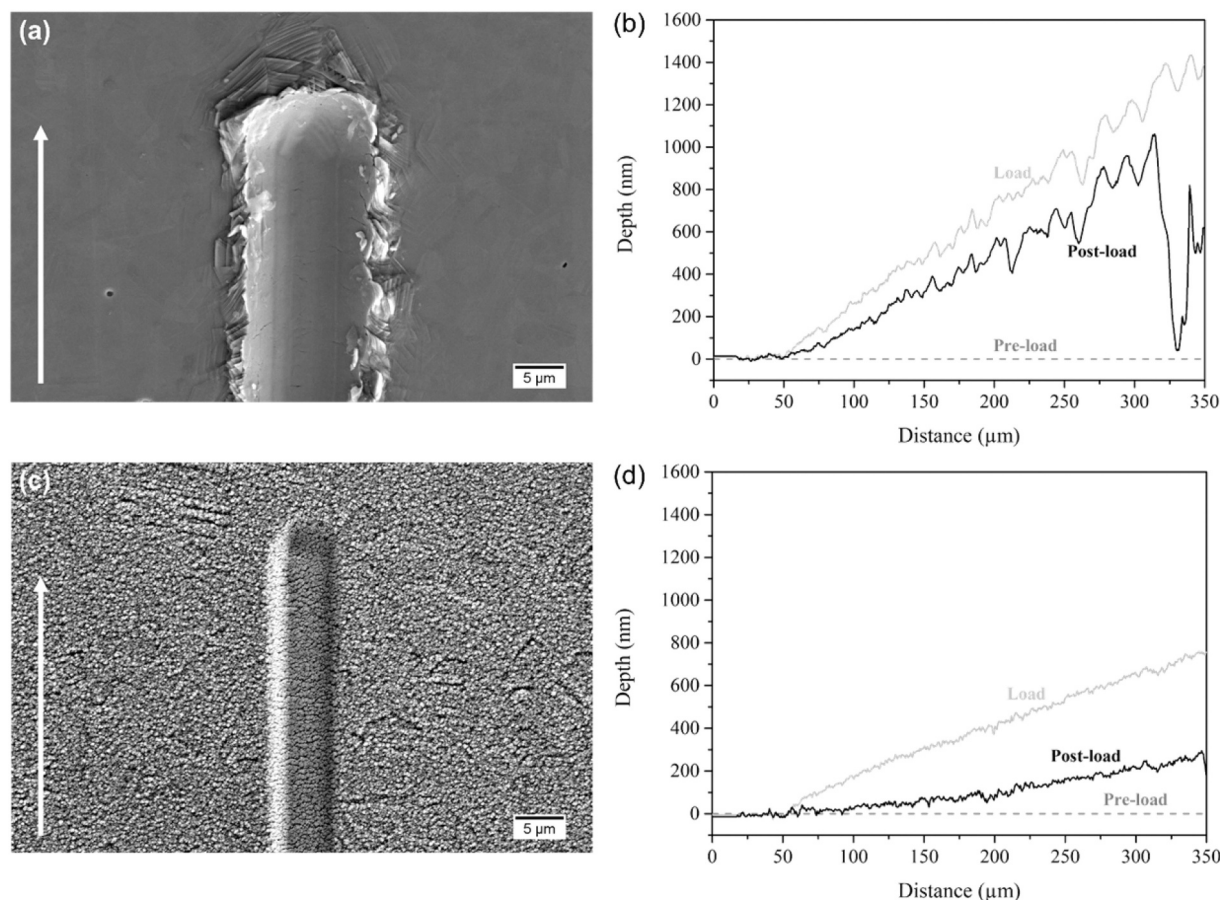
Fig. 3. (a) Secondary electron SEM micrograph showing nano-scratch of uncoated CoCrMo, and (b) the corresponding nano-scratch profile for uncoated CoCrMo; (c) Secondary electron SEM micrograph showing nano-scratch of coated CrN/S CoCrMo, and (d) the corresponding nano-scratch profile for coated CrN/S CoCrMo. The arrows indicate the direction of sliding.

with a three-electrode setup; the sample acting as the working electrode, a platinum-coated titanium rod used as the counter electrode and a saturated calomel electrode (SCE) as the reference electrode. This setup was connected to a Gamry Reference 1000™ potentiostat (Gamry, USA) to program and monitor the electrochemical processes during the tests.

Prior to each test, both the disc and ball forming the tribopair were immersed in IPA and placed in an ultrasonicator for 15 min for cleaning. These were then allowed to dry and were mounted in the tribocorrosion tester. The electrochemical cell was filled with 300 mL of electrolyte (Ringer's solution or diluted FBS) which was maintained at 37 ± 1 °C. The tribopairs (uncoated disc vs. uncoated ball and coated disc vs. coated ball) were then made to slide against each other at a stroke length of 6.5 mm and a frequency of 1 Hz. The applied normal load used was 3 N for a sliding duration of 7200 s. The dynamic friction coefficient generated during sliding was measured using an SP22 load transducer (Amber Instruments Ltd., UK) and recorded using Labview software. The CrN/S coated samples were also tested for a longer duration of 24 h under the same conditions in both Ringer's solution and dilute FBS.

The contact pressures in a MoM hip joint produced under standard walking conditions are generally <100 MPa, however, much larger contact stresses could result due to micro-separation [27]. In this work a normal load of 3 N, which results in an initial contact stress of 630 MPa for the uncoated tribopair, was used. This contact stress produces a maximum subsurface shear stress of 190 MPa. Therefore, gross plastic deformation of the substrate material is not expected to occur since the shear yield strength approximated using Tresca criterion of the CoCrMo disc, which is 500 MPa, is not exceeded [28]. The loading conditions used in this study enabled for measurable losses within a reasonable time and the tribocorrosion evaluation of the coating under a more

severe contact condition which increases their propensity to failure [24].

Tribocorrosion tests of the uncoated-on-uncoated and coated-on-coated tribopairs were conducted under anodic potential (AP) conditions of +100 mV vs. SCE. In this case, the evolution of the OCP was considered in determining the anodic potential used for tribocorrosion testing. The potential was selected to be 150 mV higher than the highest stable OCP measured prior to sliding in either Ringer's or FBS. In this work, the highest stable OCP recorded was about −50 mV for CrN/S in Ringer's solution. The generated anodic current during testing under AP conditions is associated with the amount of dissolution/oxidation of the material and can also be used for the quantitative determination of material losses via corrosion and wear-enhanced corrosion (C_W) using Faraday's law.

Initially, the disc sample was monitored for 600 s at the set potential without sliding. This was followed by 2 h of sliding. The dynamic co-efficient of friction and anodic current were measured during the sliding period. When sliding was ceased, the worn disc was left for another 600 s at the set potential. Tribocorrosion tests were repeated three times.

The topography of the resultant scars on the discs and counterfaces were further analysed using a light optical microscope operated in bright field mode. Tribocorrosion damage on the metallic discs and counter-faces were examined in greater detail with the FEG-SEM equipped with an Energy Dispersive Spectroscopy (EDS) detector to determine the chemical composition of any wear debris. The cross-sectional area of the tribocorrosion scar was determined by measuring the cross-section of the wear track using a profilometer equipped with a conical-shaped stylus having a radius of 1 μm. The cross-sectional area of each wear scar was calculated at three different locations from 2D profilometer
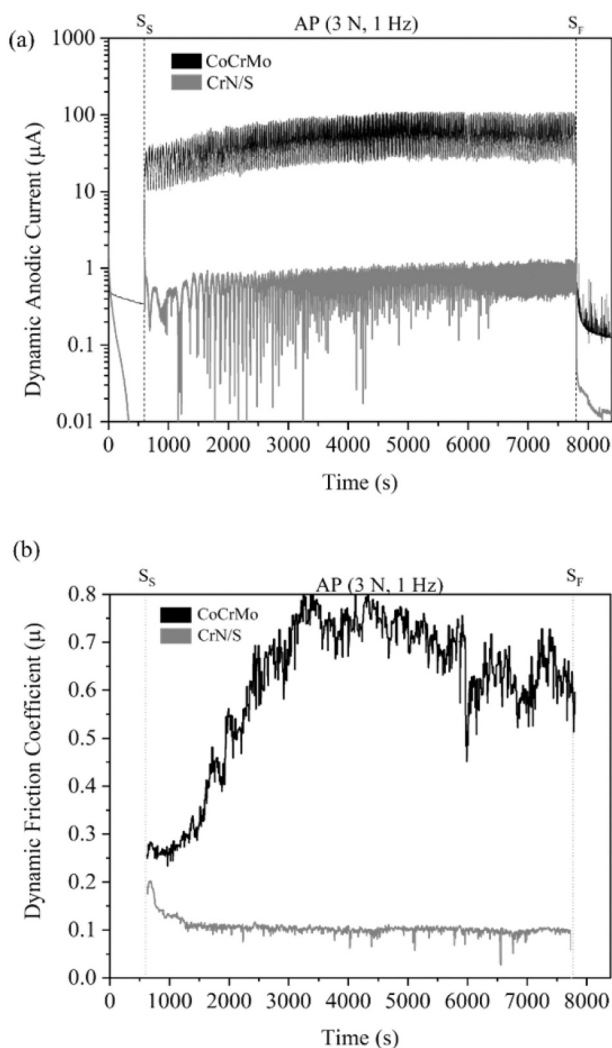
Fig. 4. (a) The dynamic anodic current against time and (b) Dynamic coefficient of friction traces following tribocorrosion tests under anodic potential (+100 mV vs. SCE) conditions in Ringer's solution. Note that the dynamic anodic current against time is plotted on a log scale. S_S and S_F represent the start and finish of sliding, respectively.

profiles (at the edges and centre of the wear scar) using Simpson's rule and then multiplied the average cross-sectional area by the length of the scar to determine the volume. The average volume lost for each tribopair was based on three repeats. The total volumetric losses were calculated using a method described elsewhere [21].

Cross-sectional analysis was also carried out on the resultant tribocorrosion scars of the uncoated CoCrMo and CrN/S coated discs following reciprocating sliding tribocorrosion tests. This was done with a FEI Nova600 Dual Beam incorporating a focused ion beam (FIB) and a high-resolution FEG-SEM and using the same procedure mentioned in Section 2.3. EDS maps were obtained using an accelerating voltage of 15 kV, current of 1.6 nA and a working distance of 5 mm.

3. Results

3.1. Coating crystal structure and morphology

Bragg-Brentano X-ray diffraction (XRD) patterns characterising the CoCrMo alloy, given in Fig. 1a, have shown that the material is composed of two different phases, namely the FCC phase (or α-phase) and the hexagonal close packed (ε-phase or HCP). The crystal structure

of the outer layer of the CrN/S coating was determined using XRD in GIAB configuration. In this configuration, the shallow penetration depth of the beam coupled with its large coverage resulted in a strong signal from the outer CrN coating with no contribution from the underlying sublayers and substrate. As shown in Fig. 1b, the outer CrN layer had a cubic NaCl prototype crystal structure with characteristic CrN (111), (200), (220), (311), (222), (400), (331) and (420) reflections. Previous XRD analysis carried out on a CoCrMo(C) layer deposited within the same chamber under conditions yielding a lower carbon concentration to those reported in Table 3 exhibited broad reflections corresponding to the cubic lattice of CoCrMo matrix carbon S-phase [17].

A secondary electron image of the fractured cross-section morphology of the CrN/S coating and an ion image of the FIB section of the coating are shown in Fig. 2a and b, respectively. The presence of the top CrN layer followed by a Cr interlayer, the CoCrMo(C) layer and the Cr adhesion layer adjacent to the substrate are distinguished on both images. The CrN layer had a fine columnar fracture morphology, typical of conventional magnetron sputtered PVD deposited nitride coatings [29]. The CoCrMo(C) comprised a dense fine columnar morphology with a transition to a largely featureless morphology towards its top. The chemical composition of each layer in the dual layer CrN/S coating is given in Table 3 while the thicknesses of the coating layers as determined from the fractured surfaces (Fig. 2a) and the surface roughness values (R_a and R_q) for both the CoCrMo coated discs and spheres are given in Table 4. The thickness of the coating layers was also found to be in agreement with the FIB cross-sections (Fig. 2b).

3.2. Nano-hardness and nanoscratch testing

The nano-indentation hardness of the CrN/S coated CoCrMo discs was 20.1 ± 1.7 GPa while the nano-hardness of the underlying CoCrMo (C) S-phase layer was measured to be 12.7 ± 0.3 GPa in a previous study [17] conducted by the authors using the same PVD chamber and same target configuration but using a lower methane to argon flow ratio yielding a lower carbon concentration in the coating. A higher carbon concentration is expected to further contribute to coating hardness and load bearing capabilities. The role of the underlying CoCrMo(C) layer was to produce a good load support to the top CrN layer. It is also to be noted that the measured nano-indentation hardness of the uncoated CoCrMo discs (8.1 ± 0.3 GPa) and uncoated CoCrMo balls (7.1 ± 0.5 GPa) appear to be somewhat overestimated. The reason could lie in the fact that the "compliance" of nano-hardness machines needs to be "very stiff" for it to accurately determine very small depth displacements (<200 nm) of high-hardness materials (~15 GPa) [19]. As a consequence, the nano-hardness values measured for materials such as CoCrMo alloys, austenitic stainless steels and Ti-6Al-4V of moderate hardness (~5 GPa) are overestimated [19].

Nano-scratch tests showed that the uncoated CoCrMo exhibited plastic deformation with material build up on the sides of the scar and in front of the indenter (Fig. 3a). Material was ploughed with the indenter as it moved resulting in a roughened scar with a maximum plastic depth of ~1 μm (Fig. 3b). The scar had evidence of plastic deformation but no cracking was observed both inside and outside of the scar. The resultant scars on CrN/S coated CoCrMo discs exhibited no evidence of delamination damage or coating loss (Fig. 3c), indicating an excellent adhesion between the different layers of the coating and the coating-substrate interface. The coated CrN/S disc displayed a shallower scar (0.3 μm plastic depth at maximum load) with the coating retaining its topographic features and mechanical integrity (Fig. 3c). The load and post-load scratch profile scans (Fig. 3d) revealed that some plastic flow of the inner CoCrMo(C) layer or the underlying substrate took place during scratching without substantial roughening along the scar. This scratch response shows that the coated CrN/S disc was very resistant to mechanical damage and that the top CrN layer had a good load support under the nano-scratch test conditions used, meriting further tribocorrosion evaluation.
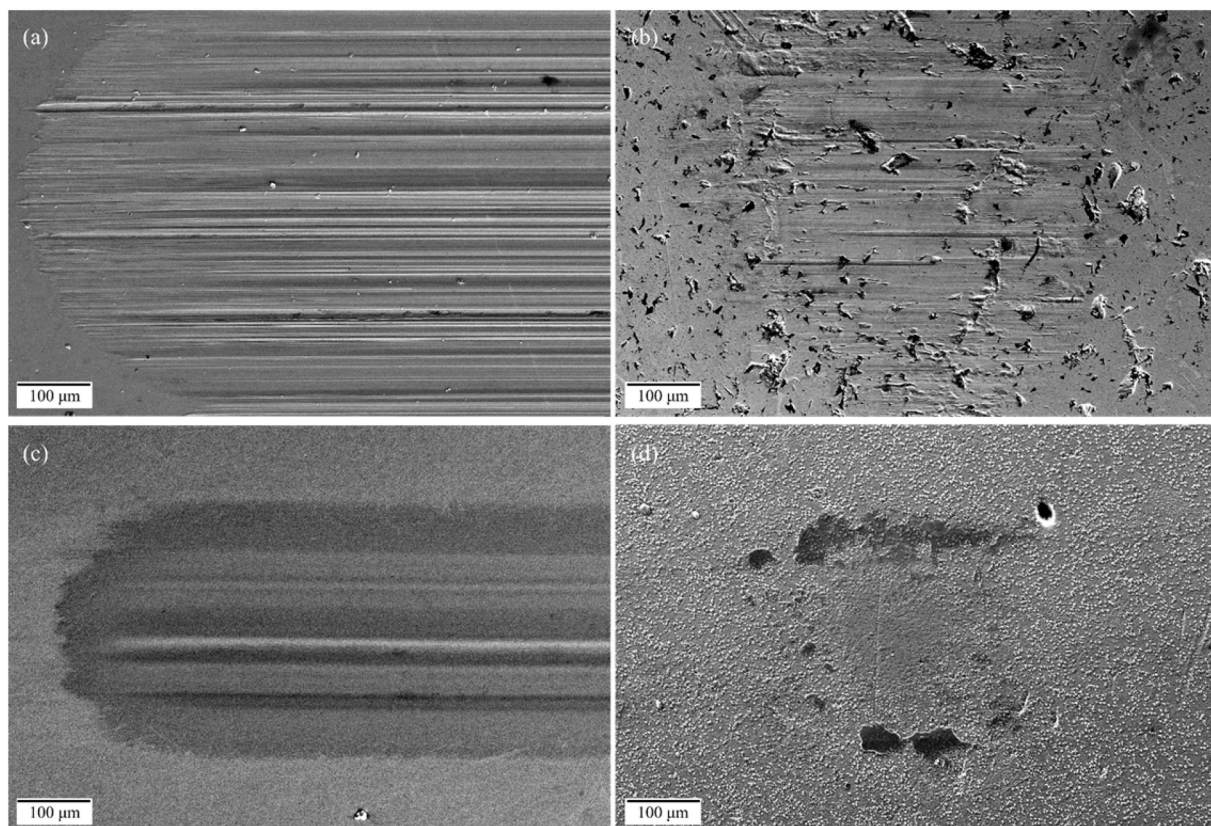
Fig. 5. Secondary electron SEM images of the tribocorrosion scars on (a) CoCrMo discs, and (b) corresponding CoCrMo counterfaces, and (c) CrN/S coated discs, and (d) corresponding CrN/S coated counterfaces following reciprocating sliding tribocorrosion tests under anodic potential conditions in Ringer's solution. Sliding direction is from left to right.

3.3. Tribocorrosion

#### 3.3.1. Electrochemical response and coefficient of friction in Ringer's solution

The evolution of the dynamic anodic current and the development of the dynamic friction coefficient for the uncoated CoCrMo and coated CrN/S tribopairs following testing under AP conditions are shown in Fig. 4. Prior to sliding initiation, the anodic current of both tribopairs stabilised at a very low anodic current (<1 µA) indicating the tribopairs were in a passive state (Fig. 4a). This was followed by an instantaneous rise in dynamic current as soon as sliding commenced. The CoCrMo tribopair experienced an abrupt rise in current which oscillated between 10 and 40 µA. The dynamic current increased gradually and displayed largest oscillations of between 25 and 110 µA at 5000 s from test commencement. It remained such until the end of the sliding period. In contrast, the CrN/S tribopair exhibited minimal rise in anodic current to about 1 µA throughout the sliding period. The dynamic anodic current of both the uncoated and coated tribopairs decreased immediately back to a very small anodic current value (<0.2 µA) when sliding was halted (Fig. 4a).

Throughout the sliding period, the uncoated CoCrMo tribopair displayed a higher COF when compared to the coated tribopair (Fig. 4b). The COF for the uncoated was ~0.25 at the start of the test and following a short period of around 600 s it started to gradually increase to a maximum of 0.8 within a period of 2000s of sliding while displaying increased fluctuations in the COF trace. The COF then trended slowly back to reach ~0.6 by the end of sliding. This friction behaviour was displayed in all repeated tests. In contrast, the COF trace of the CrN/S coated tribopair was characterised by a low (~0.1) and smooth dynamic COF trace.

3.3.2. Tribocorrosion scar morphology in Ringer's solution

Tribocorrosion scars following testing of CoCrMo and CrN/S tribopairs under anodic potential conditions in Ringer's solution are shown in Fig. 5. The scar on the CoCrMo disc featured several grooves aligned along its length, with some fine oxidised debris (37.6 at.% O, 31 at.% C, 16 at.% Co, 13.2 at.% Cr and 1.5 at.% Mo) adhering to the sides of the scar (Fig. 5a). The scar profile presented in Fig. 6a shows that the scar was ~5.5 µm deep and that it contains numerous grooves which were largely <1 µm in depth. Material transfer or detachment via adhesive wear was not evident on both tribopair surfaces. In contrast, the scar on the CrN/S coated disc had a largely featureless and polished topography (Fig. 5c) with few shallow grooving marks aligned along the sliding direction (Figs. 5c and 6a) and having a scar depth of ~0.5 µm. No debris could be observed on the scar of the CrN/S coated disc, however, the corresponding CrN/S coated counterface (Fig. 5d) consisted of very fine agglomerated oxidised debris (45.4 at.% O, 10.9 at.% C, 26.3 at.% Cr and 17.4 at.% N) around the scar.

The width of the ball scars corresponds to the width of the scar on the disc. The elliptical shape of the scar images (Fig. 5b, d) and their spherical profile (Fig. 6b) show that material was being largely lost from the disc while the balls were retaining conformity with the disc scar. Micro-grooving marks in the sliding direction were observed within the scar of the uncoated CoCrMo ball (Fig. 5b). Higher magnification SEM imaging of the ball scar revealed numerous comet scratches aligned with the direction of motion. These scratches often coincided or terminated with micropores. These scratches had widths of similar dimensions to the diameter of these micropores which in turn had dimensions similar to those observed within the crystallites in the material microstructure (Section 2.1). Such micro-scratches were more intense in regions adjacent to bigger pores within the scar. The latter pores were observed to happen within the continuous phase in the microstructure (Section 2.1).
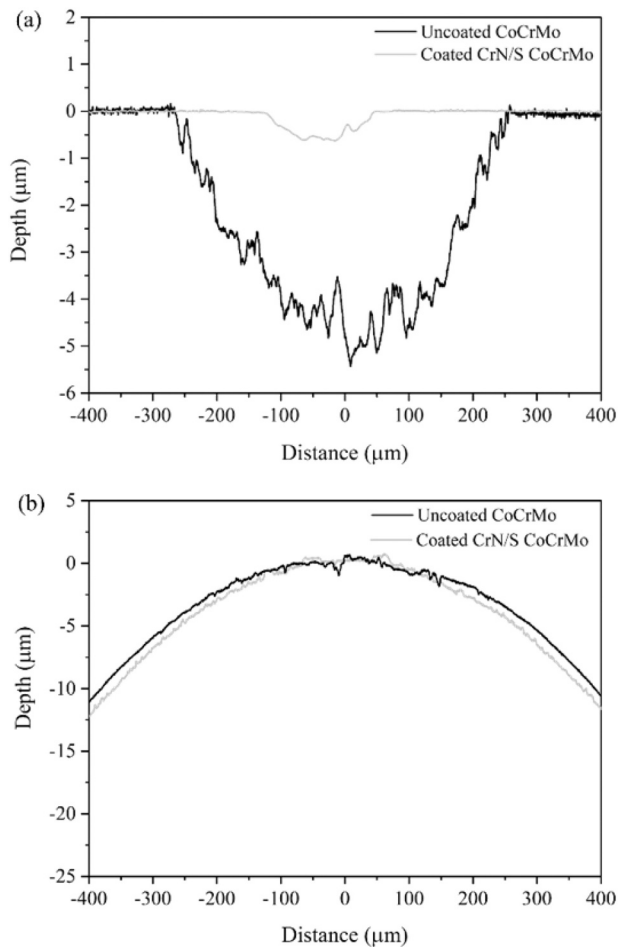
Fig. 6. 2D scar profiles for the uncoated CoCrMo and coated CrN/S CoCrMo (a) discs and (b) counterfaces after tribocorrosion testing in Ringer's solution.

The continuous phase appeared to be more resistant to scratching when compared to the crystallites. Both types of pores were also present outside of the scar. Submicron oxidised metallic debris was present within the scar. In contrast, the CrN/S coated ball (Fig. 5d) displayed a smoothened topography with some of the original coating micro-topographic features still visible within the scar. Fine metal oxide wear debris (45.4 at.% O, 10.9 at.% C, 26.3 at.% Cr and 17.4 at.% N), probably consisting of fine debris agglomerated together, was adhered to the edges of the scar (Fig. 5d).

3.3.3. Electrochemical response and coefficient of friction in diluted FBS

Fig. 7 illustrates the dynamic anodic current and dynamic friction coefficient as a function of time for tribocorrosion tests of the uncoated CoCrMo and coated CrN/S tribopairs in dilute FBS. For both tribopairs, the anodic current stabilised at ~0.1 μA following the application of the anodic potential. When sliding was initiated, the dynamic current exhibited a sharp increase for both tribopairs albeit to one different order of magnitude (Fig. 7a). The current trace for the uncoated CoCrMo tribopair oscillated between 7 and 24 μA throughout the sliding period. In contrast, the current trace for CrN/S decreased from 3 to 0.7 μA during the first few minutes of sliding and then oscillated about 0.7 μA until the end of the sliding period. For both tribopairs, the current dropped abruptly to ~0.1 μA when sliding was stopped.

CrN/S displayed an average COF of ~0.06 which was stable throughout the sliding period and comparable to tests carried out in Ringer's solution. The CoCrMo tribopair exhibited a constant COF of ~0.14 (Fig. 7b) which was much lower to tests carried out in Ringer's solution. Both samples displayed smooth and stable COF traces
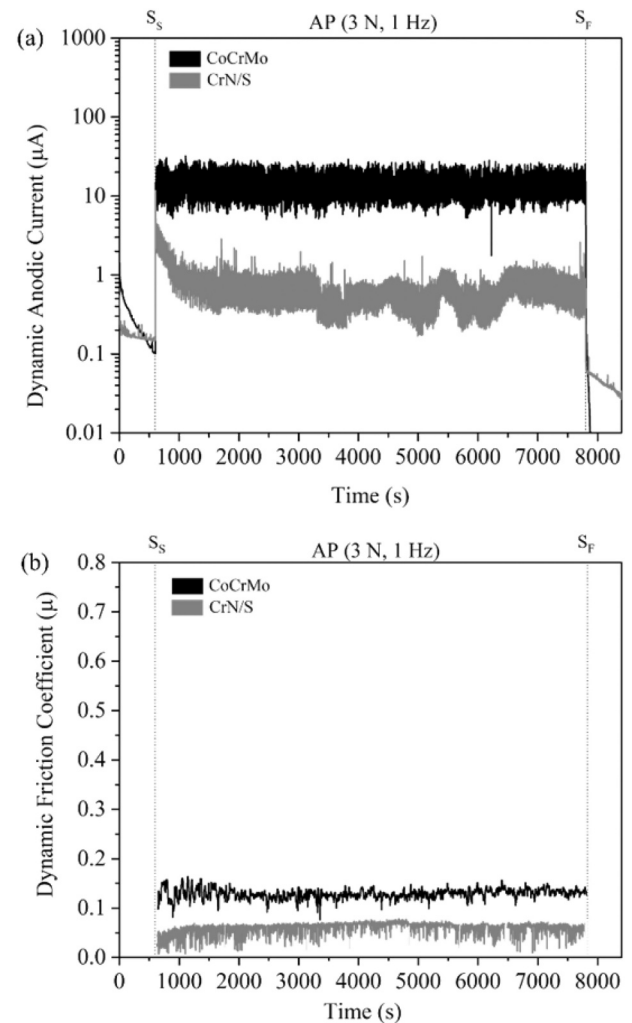
Fig. 7. (a) The dynamic anodic current against time and (b) Dynamic coefficient of friction traces following tribocorrosion tests under anodic potential (+100 mV vs. SCE) conditions in FBS. Note that the dynamic anodic current against time is plotted on a log scale. S_S and S_F represent the start and finish of sliding, respectively.

throughout the sliding period.

3.3.4. Tribocorrosion scar morphology in diluted FBS

SEM images of the scars on CoCrMo and CrN/S tribopairs following tribocorrosion testing under anodic potential conditions in FBS are shown in Fig. 8. Several micro-grooving marks aligned along the sliding direction were observed using SEM within the scar on the uncoated CoCrMo disc (Fig. 8a). The 2D profile (Fig. 9a) across the scar shows the grooving marks to be similar in number but generally deeper than the ones observed following tests in Ringer's solution (Fig. 6a). Here (Fig. 9a) the maximum scar depth was ~3 μm which was less than the corresponding scar produced in Ringer's solution. The CrN/S coated disc exhibited negligible damage in the form of polishing (Fig. 8c) and a 2D profile trace across the scar could hardly distinguish its presence (Fig. 9a).

The wear scar on the CoCrMo ball (Fig. 8b) was larger with respect to that on the CrN/S coated ball (Fig. 8d) as expected from the corresponding scars on the discs. Similar to the uncoated CoCrMo scar observed in Ringer's solution, numerous micro-abrasion marks were observed together with the presence of micro-pores (Fig. 8b). The 2D profilometry trace across the scar on the CoCrMo ball (Fig. 9b) showed that the contact area retained sphericity but had a roughness that
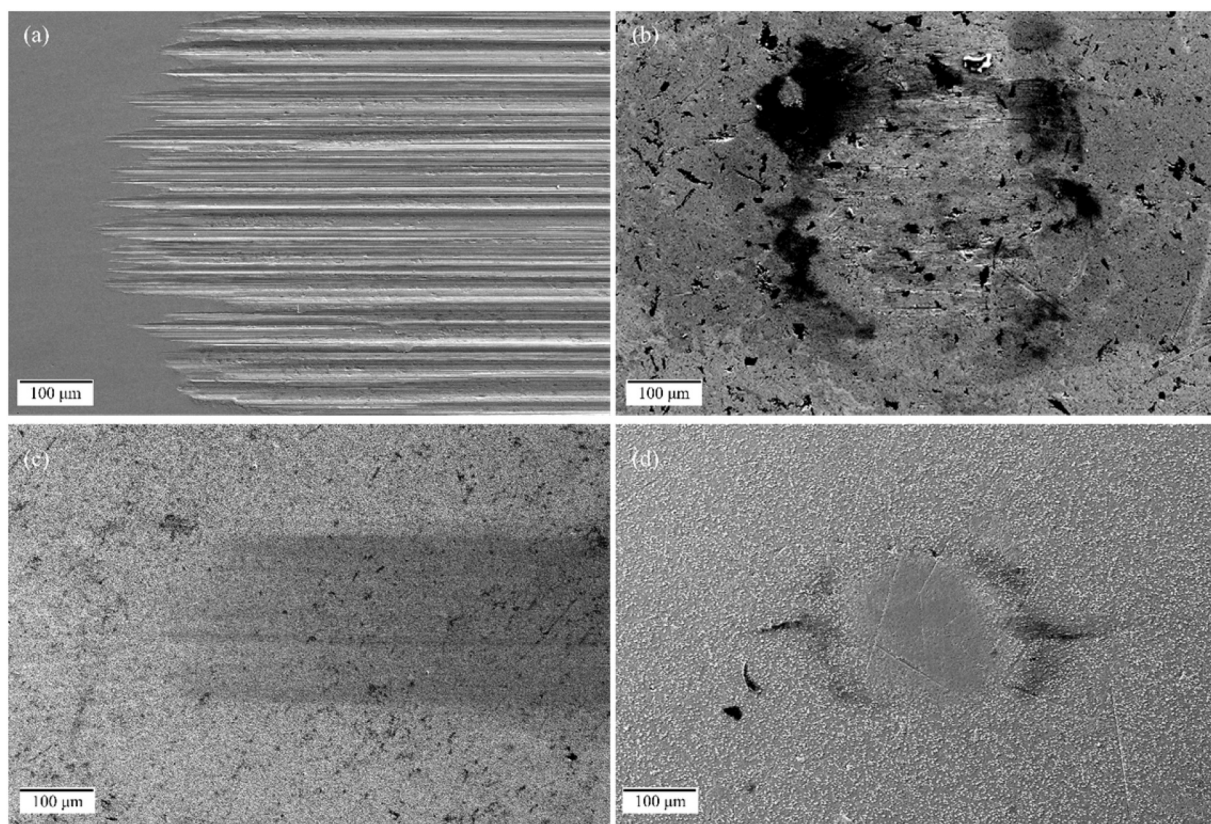
Fig. 8. Secondary electron SEM images of the tribocorrosion scars on (a) CoCrMo discs, and (b) corresponding CoCrMo counterfaces, and (c) CrN/S coated discs, and (d) corresponding CrN/S coated counterfaces following reciprocating sliding tribocorrosion tests under anodic potential conditions in FBS. Sliding direction is from left to right.

conforms with that of the corresponding disc. Black deposits, characterised as oxidised agglomerated debris (37.5 at.% O, 35.8 at.% C, 10.7 at.% Co, 10.2 at.% Cr and 0.9 at.% Mo), were also detected at the edges of the wear track. The scar on the CrN/S coated ball was featureless and had a polished appearance (Fig. 8d). The contact area retained its original sphericity (Fig. 9b). A small amount of fine debris was adhered to the sides of the scar (12.5 at.% O, 19.2 at.% C, 33.8 at.% Cr and 32.2 at.% N).

3.3.5. Total volume losses

Faraday's law was used to determine the volumetric losses due to wear-enhanced corrosion where a molar mass, M, of 0.06 kg mol^{-1} (for uncoated CoCrMo) and 0.03 kg mol^{-1} (for CrN/S), sliding time, t, of 7200 s, Faraday's constant, F, of 96,500 C mol^{-1} and a density, ρ, of 8520 kgm^{-3} (for uncoated CoCrMo) and 5900 kgm^{-3} (for CrN/S) were used. The valence number, η, was calculated by considering the percentage content and the oxidation number of each element present at the surface of the material (from Pourbaix diagrams at a pH of 7.4 and a potential of E vs. SCE of 100 mV). The valence number, η, used for uncoated CoCrMo and CrN/S were 2.5 and 1.5, respectively.

Fig. 10 illustrates the chemically and mechanically associated volumetric losses for the uncoated CoCrMo and CrN/S coated discs following tribocorrosion testing under AP conditions. The uncoated CoCrMo material exhibited a higher material loss compared to the coated CrN/S discs for both tests in Ringer's and dilute FBS solution. The discs exhibited higher amounts of volume loss with respect to their corresponding counterfaces. The uncoated CoCrMo and coated CrN/S balls exhibited negligible material losses and their spherical profile has been preserved in both electrolytes (Figs. 6b and 9b), hence their material loss was not considered in calculating the total volume losses.

The uncoated tribopairs displayed similar material losses by wear

but testing in FBS resulted in a marked reduction in material loss by wear-enhanced corrosion. For the CrN/S, testing in diluted FBS mitigated material loss by mechanical wear while the very small chemical-associated material loss was not affected.

The maximum depths of the corrosion-wear scars following testing under AP conditions in Ringer's solution of the uncoated CoCrMo and coated CrN/S discs were measured to be 5.5 $\pm$ 0.2 μm and 0.6 $\pm$ 0.0 μm deep, respectively (Fig. 6a). Under these test conditions, the top CrN layer was never perforated. The scar for the uncoated CoCrMo disc immersed in dilute FBS had a maximum depth of 3 $\pm$ 0.3 μm (Fig. 9a). Conversely, the coated CrN/S disc exhibited negligible topographical changes in the scar such that the scar depth could not be measured (Fig. 9a). Furthermore, it is noted that no delamination of the coating and corrosion at the coating-substrate interface was evident following examination of the resultant scars in both Ringer's and dilute FBS solutions.

As shown by Stack et al. in [30], the total mass loss can be expressed in terms of the individual mass loss contributions, K_a (the mass of material removed due to wear) and K_c (the mass of material removed due to corrosion). In this work, the terms K_a and K_c are replaced by W^* and C^*, respectively (Fig. 10). The ratios, defined by Stack et al. in [30], classify the tribocorrosion regime.

3.3.6. FIB cross-sections on uncoated CoCrMo disc scars

Fig. 11a illustrates a focused gallium electron beam image of a cross-section prepared by the same ion beam towards the middle of the uncoated CoCrMo scar produced during testing in Ringer's solution. The section is oriented in the longitudinal direction. The section shows the grain structure of the CoCrMo in the as-delivered condition extends to the surface of the section indicating that there was no plastically refined zone on the micron level (Fig. 11a). The absence of a refined or mixed
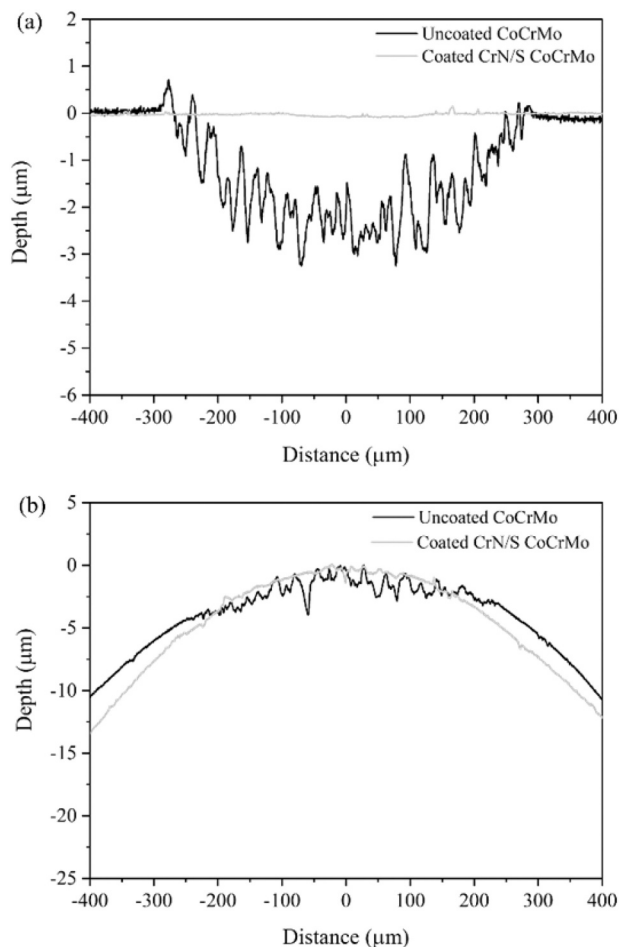
Fig. 9. 2D scar profiles for the uncoated CoCrMo and coated CrN/S CoCrMo (a) discs and (b) counterfaces after tribocorrosion testing in diluted FBS.
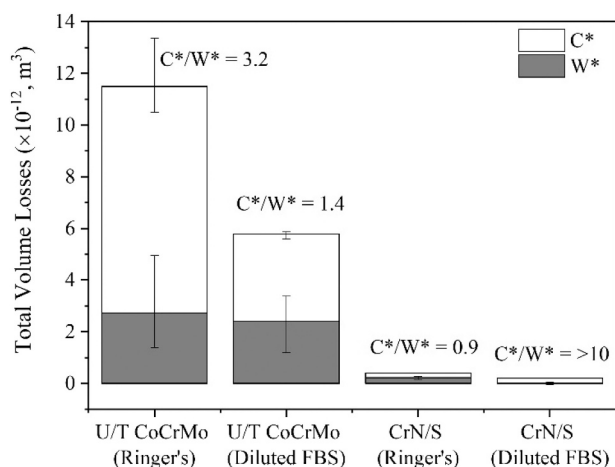

Fig. 10. Tribocorrosion volumetric losses for CoCrMo and CrN/S discs using the synergistic approach. C^* is the total volume lost due to corrosion which is assumed to be equal to wear accelerated corrosion (C_W) for passive materials. W^* is the total volume loss due to wear calculated by subtracting the measured volume loss from C_W. Error bars represent the maximum and minimum values of three repeats.

and oxidised zone inside the scar can also be noticed from a top-view ion image carried out on the same uncoated CoCrMo scar (Fig. 11b) and from its corresponding carbon (Fig. 11c) and oxygen (Fig. 11d) EDS

maps. The EDS maps clearly show that there is no difference in oxygen and carbon content outside and inside the scar. The absence of a tribo-logically transformed layer is a further confirmation that the load used in this study resulted in elastic stresses. This result contrasts to published work where high contact loads inducing plastic deformation were used [31].

Similar to the tests carried out in Ringer's solution, no refined or mixed zone could be observed at the sub-microstructure beneath the scar of the uncoated CoCrMo alloy following testing in diluted FBS. It is also important to note that, for the tests carried out in the presence of diluted FBS, it was not possible to determine any adsorbed protein-rich layers in the range of a few nanometres. This can also be corroborated with EDS analysis carried out at the surface of the uncoated CoCrMo scar with the following elemental composition; 12.1 at.% C, 6.9 at.% O, 50.5 at.% Co, 26.2 at.% Cr and 3.0 at.% Mo. This elemental composition was very similar to the composition found at the surface of an uncoated CoCrMo scar following testing in Ringer's solution; 11.0 at.% C, 1.3 at.% O, 54.8 at.% Co, 28.1 at.% Cr and 3.2 at.% Mo. The similar carbon contents imply that the presence of a protein-rich layer, if any, on the scars tested in diluted FBS must be very thin.

### 3.4. CrN/S tribopair response to 24 h tribocorrosion tests under AP conditions

3.4.1. Electrochemical response and coefficient of friction
The dynamic anodic current and dynamic coefficient of friction traces for the CrN/S coated tribopairs obtained during tribocorrosion testing in Ringer's solution and diluted FBS are presented in Fig. 12. Upon sliding initiation, the dynamic anodic current of the CrN/S coated tribopair increased to ~1 μA and 0.5 μA when testing in Ringer's solution and diluted FBS respectively (Fig. 12a). The coated tribopairs tested in diluted FBS exhibited a stable dynamic anodic current trace throughout the sliding duration. In Ringer's solution, two minor spikes in anodic current could be observed at 4 h (~5 μA) and 19 h (~3 μA). Upon cessation of sliding, the anodic currents of the coated tribopairs decreased to values which were observed before rubbing was started and remained stable until the end of the test.

The coefficient of friction traces for the CrN/S coated tribopairs are shown in Fig. 12b. The coated tribopairs exhibit a low and stable average dynamic COF of ~0.13 in Ringer's solution and ~0.17 in diluted FBS.

3.4.2. Tribocorrosion scar morphology
SEM images of the resultant scars on the CrN/S coated discs and CrN/S coated counterfaces following tribocorrosion testing for 24 h under anodic potential conditions in Ringer's solution and diluted FBS are presented in Fig. 13. In contrast to the 2 h duration tests, the scar morphology of the CrN/S coated disc and CrN/S coated counterface tested in Ringer's solution for 24 h exhibited several grooving marks aligned with the sliding direction (compare Fig. 13a,b with Fig. 5c,d). Areas within the scar of the CrN/S coated disc exhibited micro-cracking and delamination (Figs. 13a and 14a). EDS mapping confirmed a higher amount of nitrogen in the regions that were not delaminated (Fig. 14b) and a higher chromium and oxygen concentration in the delaminated regions (Fig. 14c, f). Slightly higher levels of cobalt (Fig. 14d) and mo-lybdenum (Fig. 14e) were also observed in the delaminated regions. EDS results show that only the top CrN layer was removed in the damaged areas exposing the underlying Cr interlayer (Fig. 2). A FIB cross-section was prepared across the surface microcracks (i.e., parallel to the sliding direction), as shown by the broken red line in Fig. 14a. The resultant milled cross-section is presented in Fig. 15a. It was evident that the surface microcracks did not propagate into the underlying CoCrMoC layer but propagated horizontally underneath the surface resulting in delamination of the outermost CrN layer and exposure of the underlying Cr interlayer (Fig. 15b). No coating delamination was observed on the CrN/S coated counterface (Fig. 13b) and it was confirmed by EDS analysis that the topmost CrN layer was still present.
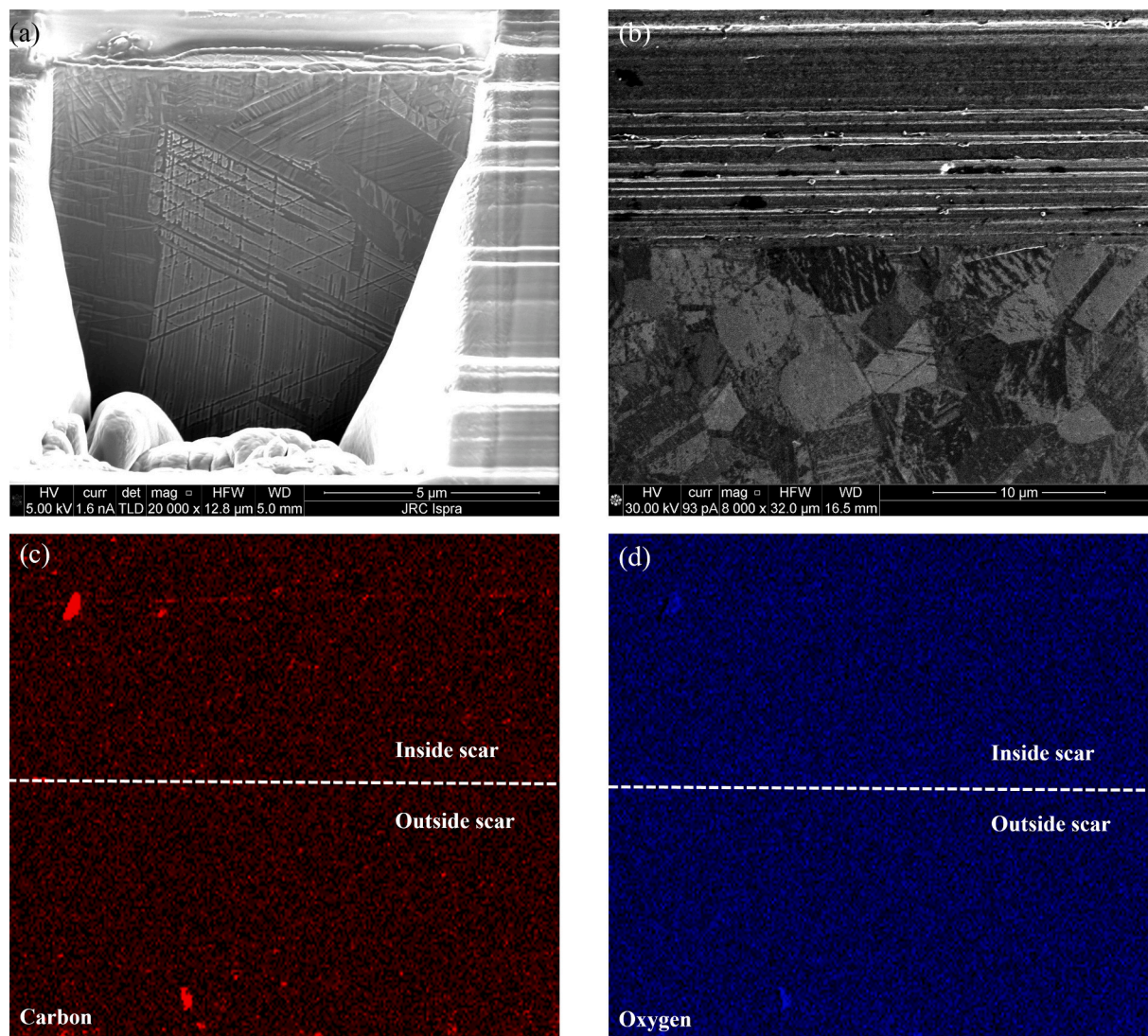
Fig. 11. (a) Secondary electron SEM micrograph of a milled cross-section inside the scar of the uncoated CoCrMo disc following tribocorrosion testing under AP conditions in Ringer's solution, (b) Focused gallium ion beam image of the uncoated CoCrMo disc following tribocorrosion testing under AP conditions in Ringer's solution, and the corresponding EDS maps showing the (c) carbon and (d) oxygen content. Sliding direction if from left to right.

The morphology of the CrN/S coated disc and CrN/S coated counterface tested in diluted FBS for 24 h exhibited a polished scar morphology (Fig. 13c, d). The coating, on both the disc and counterface, did not show any evidence of microcracking or blistering throughout the scar. The depth of the resultant tribocorrosion scar of the CrN/S coated disc tested in diluted FBS was around 0.3 μm while that of the CrN/S coated disc in Ringer's solution was about 2.5 μm (Fig. 16a). The resultant scar depths show that the remaining CrN thickness on the disc tested in Ringer's solution was very thin (Table 4) on some areas and almost completely worn away. This would explain why micro-cracks could be observed on the disc immersed in Ringer's solution while no cracks were noted on the CrN/S coated disc tested in diluted FBS as only a small fraction of the coating was worn away in case of the latter. The 2D profilometry trace across the scar on the CrN/S ball in Ringer's solution (Fig. 16b) showed that the contact area retained sphericity but had a roughness that conforms with that of the corresponding disc. In contrast, the scar on the CrN/S coated ball in FBS was featureless and had a polished appearance (Fig. 13d). The contact area retained its original sphericity (Fig. 16b).

4. Discussion

CrN/S coated tribopairs exhibited a drastic reduction in volume losses, when compared to the uncoated CoCrMo tribopairs, during tribocorrosion testing in both Ringer's and diluted FBS (Fig. 10). The coating design allowed for excellent damage resistance as displayed during nano-scratch testing (Fig. 3c, d). Furthermore, the coatings exhibited no delamination or micro-cracking following 2 h of reciprocating sliding (Figs. 5c, d and 8c, d). Long duration 24-h tests resulted in some regions on the disc which exhibited micro-cracking and delamination of the topmost CrN layer only when testing in Ringer's solution (Fig. 13a). The thinning of the top CrN layer was accompanied by development of micro-cracks oriented perpendicular to the sliding direction. Nevertheless, the micro-cracks did not penetrate through the underlying layer to the substrate (Fig. 15) and mitigated the possibility of Type II damage [22] at the coating-substrate interface – a detrimental form of tribocorrosion damage for coated metallic materials. Testing in dilute FBS resulted in a reduction in the tribocorrosion volume losses for both tribopairs compared to Ringer's solution (Fig. 10). The reduction was more pronounced for the uncoated CoCrMo tribopairs.

In Ringer's solution, the uncoated tribopair exhibited an abrupt increase in anodic current to ~25 μA at the onset of sliding and the
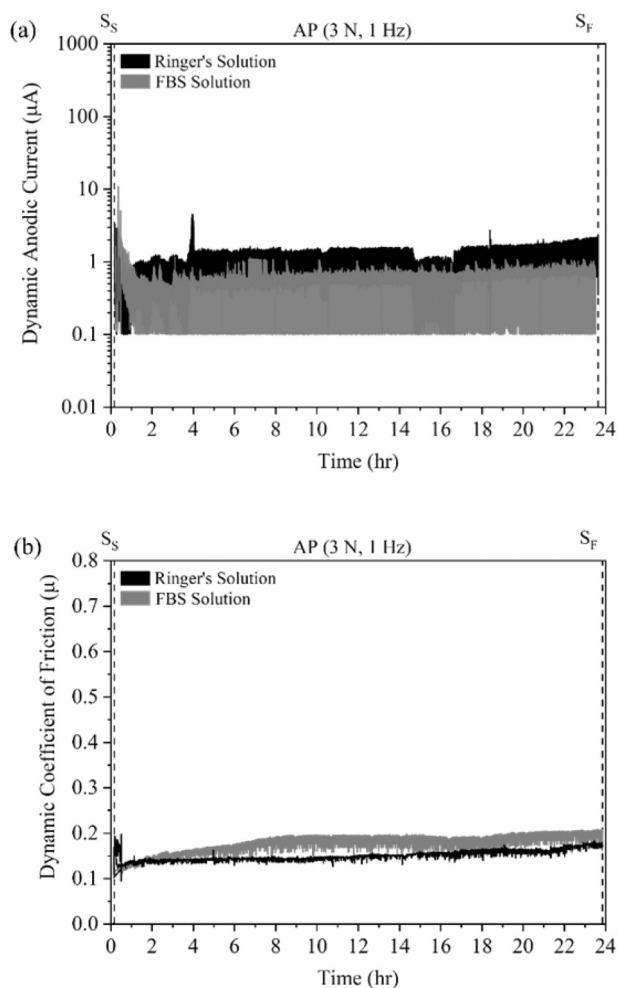
Fig. 12. (a) The dynamic anodic current against time and (b) Dynamic coefficient of friction traces following tribocorrosion tests under anodic potential (+100 mV vs. SCE) following reciprocating sliding tribocorrosion tests of CrN/S for 24 h conditions in Ringer's solution and diluted FBS. Note that the dynamic anodic current against time is plotted on a log scale. S_S and S_F represent the start and finish of sliding, respectively.

dynamic COF was ~0.27 for the first few minutes of sliding (Fig. 4). The increase in anodic current was the result of the rubbing action between the disc and the counterface ball which resulted in damage to the passive film - the latter providing a kinetic barrier to corrosion for the CoCrMo alloys. Such damage is followed by ion dissolution and re-passivation, both contributing to the measured anodic current. This tribocorrosion mechanism is widely reported in literature and has been referred to as Type I corrosion-wear [17,21,22]. It accounted for the biggest material loss component for the tests conducted in Ringer's solution (Fig. 10). The anodic current started to increase markedly following a brief period of sliding and exhibited increased level of fluctuations (Fig. 4a). Similarly, the dynamic COF trace increased to a maximum of ~0.8 and exhibited increased fluctuations (Fig. 4b). The disc and ball scar morphologies displayed abrasive damage in the form of grooves aligned with the direction of sliding (Fig. 5a, b). The presence of chromium-rich and molybdenum-rich phase constituents identified in the ball material (Section 2.1, Fig. 17) were observed to be more abrasion damage resistant compared to the rest of the microstructure as evidenced by their general higher resistance to micro abrasion damage. It is expected that the wear across the multi-phase ball microstructure was uneven. This would result in the chromium-rich and molybdenum-rich micro-constituents, residing in the crystallite boundaries, to protrude from the surface causing increased two-body damage to the disc material and

contributing to both an increased anodic current and friction (Figs. 4 and 17). Furthermore, regions adjacent to the larger (~20 μm) pores within the ball scars exhibited high density of comet-like scratch damage (Fig. 5b) aligned with the direction of motion. This type of scratch damage suggests that micro-fragmentation of hard particles, facilitated at pore periphery, occurred at some juncture, creating a source of fine debris resulting in three-body abrasion damage. Fine oxidised and agglomerated metallic debris may also have contributed to three-body damage. Therefore, during tribocorrosion testing, roughening of the counterface material leading to an increased damage to the disc, a process analogous to Type III corrosion-wear [22], is likely to have occurred and explains the higher material losses exhibited by the disc compared to the ball. There was no evidence of adhesive type damage in the ball and disc wear scars and hence the evolution of the scar morphology and the presence of third body particles were likely responsible for the increased magnitude and fluctuations in both anodic current and friction. Wear accelerated corrosion was the principal loss mechanism followed by wear via abrasion damage. The friction and current remained rather high till the end of sliding suggesting that a tribolayer that mitigates material losses was not produced. The absence of a tribolayer is further supported by FIB analysis of the disc where the disc material grain morphology extended to the surface and EDS mapping results showed similar oxygen and carbon concentrations for the regions inside and outside the tribocorrosion scar (Fig. 11).

The addition of FBS to Ringer's solution resulted in a marked reduction in both the anodic currents (Figs. 4a and 7a) and the dynamic COF (Figs. 4b and 7b). This response is a clear indication to the formation of a relatively spontaneous film on the test surfaces which acted to both lubricate the tribological interface and mitigate anodic dissolution. Numerous researchers attributed the beneficial effect of a protein-containing electrolyte on the tribocorrosion performance of biomedical alloys to the presence of a protein-rich film [32–35]. The presence of a protein-rich film has been deemed as essential in limiting the wear of MoM bearings whereby the film may act beneficially as both the barrier to corrosion and lubricant to facilitate sliding [33]. It was also shown that under tribocorrosion conditions, the formation of organometallic complexes have a tendency to reduce friction by acting as a solid lubricant [34] and that the presence of proteins directly affects the synergism of wear and corrosion in the tribo-contact [32]. In this work, the presence of a protein-rich film could not be directly observed, but the lower dynamic anodic current and friction suggest that a very thin (nanometric) layer has formed on the surface which provided a good level of protection against ion dissolution and was a source of enhanced lubrication. In fact, despite the presence of abrasion damage and scar roughening on both the ball and disc scars, the friction coefficient and current remained stable and relatively low, probably due to the high regeneration ability of this protective film (Fig. 17).

The addition of FBS also resulted in a marked decrease in the total volumetric losses for the uncoated tribopair but deeper grooving marks within the scars resulted (Fig. 9a, b) when compared to the scars obtained in Ringer's solution (Fig. 6a, b). It is possible that the deeper grooving marks measured for the uncoated tribopair following testing in FBS were partly the result of the lower wear accelerated corrosion compared to tests in Ringer's solution. A marked reduction in oxidative losses and similar mechanical losses (Fig. 10) compared to tests in Ringer's solution resulted in the ratio of chemical to mechanical material loss components ($\frac{C^*}{W^*}$) to decrease. In Ringer's solution, the chemical and mechanical material loss components are responsible for 76% and 24%, respectively, while in FBS they are responsible for 58% and 42%, respectively (Fig. 10). The increased roughness with increased wear to corrosion dominance suggests that whereas chemical wear is rather uniform across the surface of the disc scar, mechanical material loss was occurring preferentially within existent grooving marks amplifying the roughness of the scars (compare Fig. 6a, b with Fig. 9a, b and Fig. 8a with Fig. 5a). An increasingly roughened scar morphology when testing
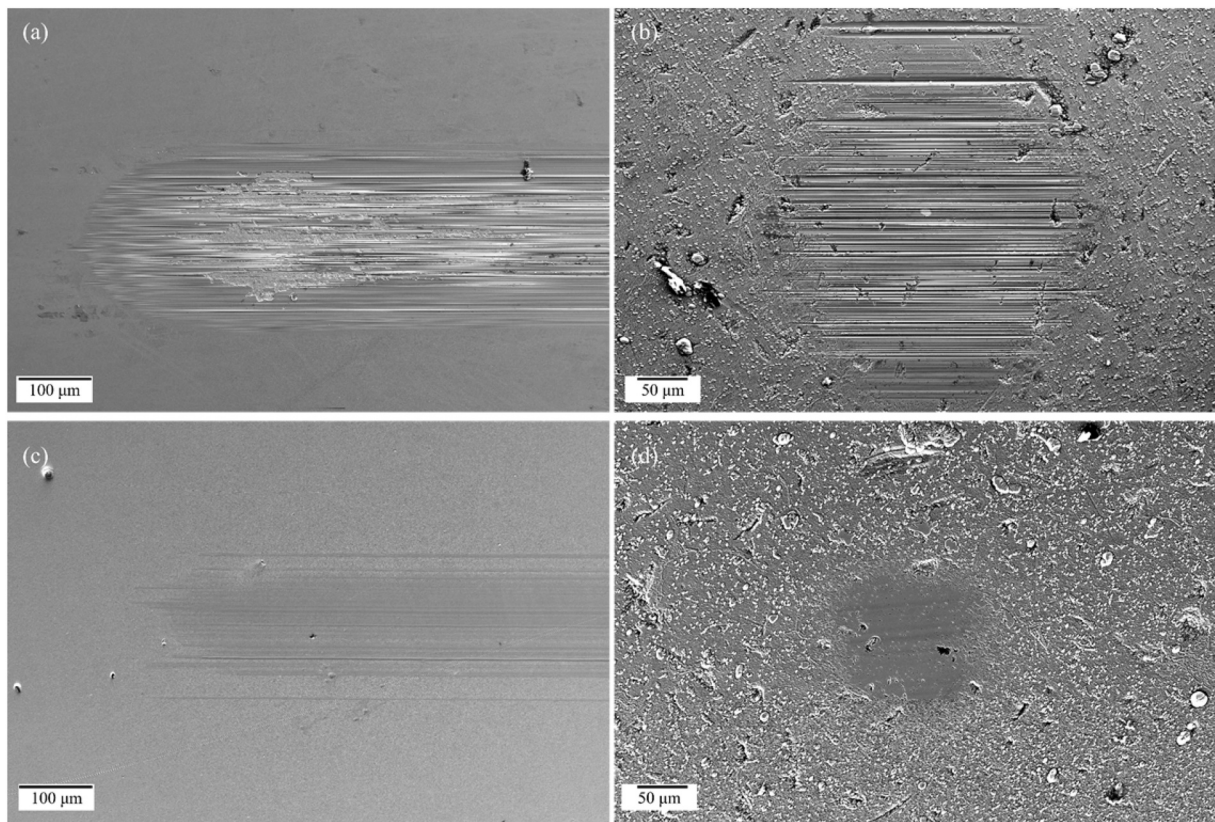
Fig. 13. Secondary electron SEM images of the tribocorrosion scars on CrN/S coated (a,c) discs, and (b,d) counterfaces, following reciprocating sliding tribocorrosion tests for 24 h under anodic potential conditions in (a-b) Ringer's solution, and (c-d) diluted FBS. Sliding direction is from left to right.
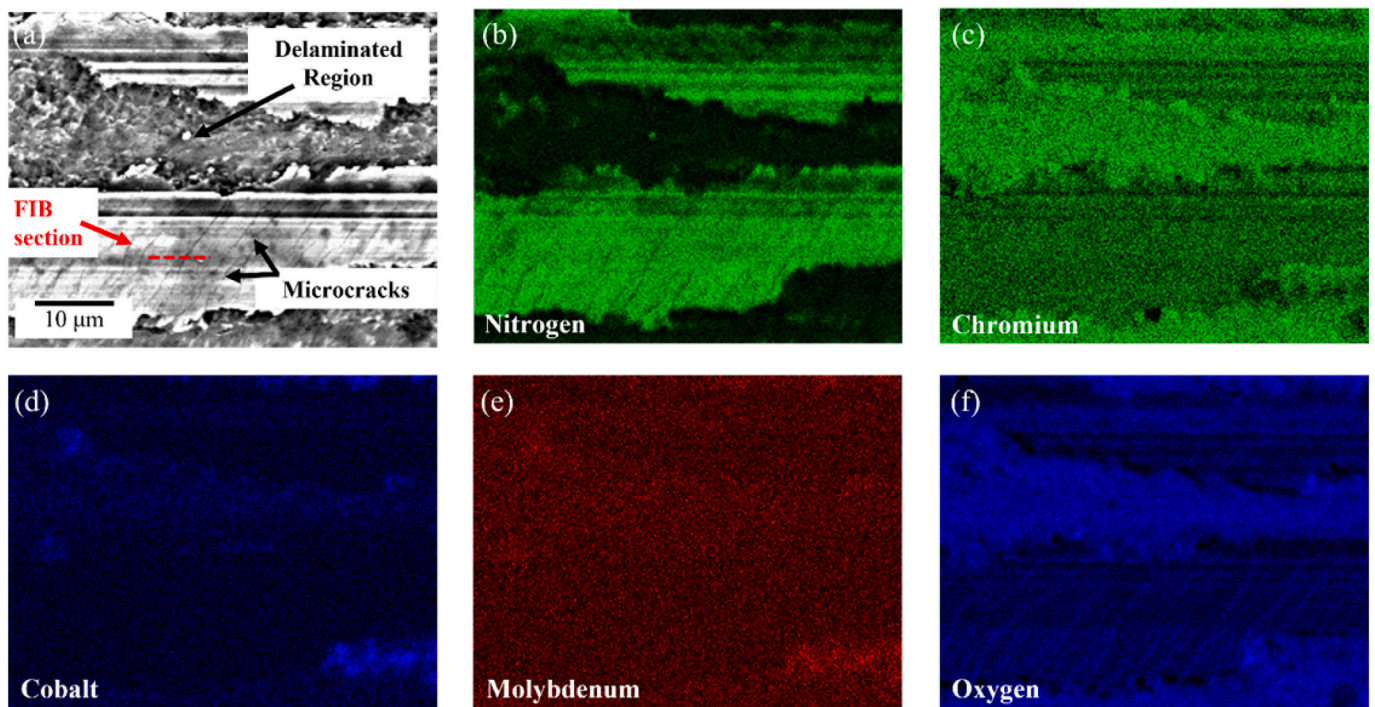
Fig. 14. (a) A high magnification corrosion-wear scar secondary electron SEM image on a CrN/S coated disc following reciprocating sliding tribocorrosion test for 24 h under anodic potential conditions in Ringer's solution showing delamination of the coating and the presence of micro-cracks. EDS mapping was carried out on this image to analyse the presence of (b) nitrogen, (c) chromium, (d) cobalt, (e) molybdenum, and (f) oxygen. Sliding direction is from left to right.
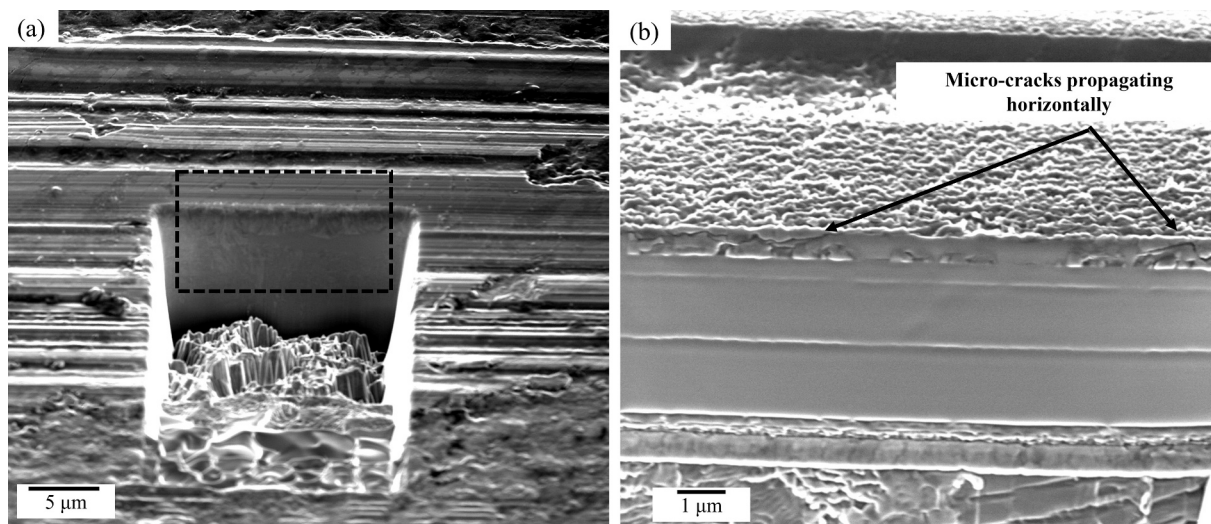
Fig. 15. (a) A secondary electron SEM image showing the area where FIB milling was carried out inside the corrosion-wear scar of the CrN/S disc following reciprocating sliding tribocorrosion test for 24 h under anodic potential conditions in Ringer's solution, and (b) a magnified secondary electron SEM image of the area in (a) showing the propagation of micro-cracks at a cross-section. Sliding direction is from left to right.
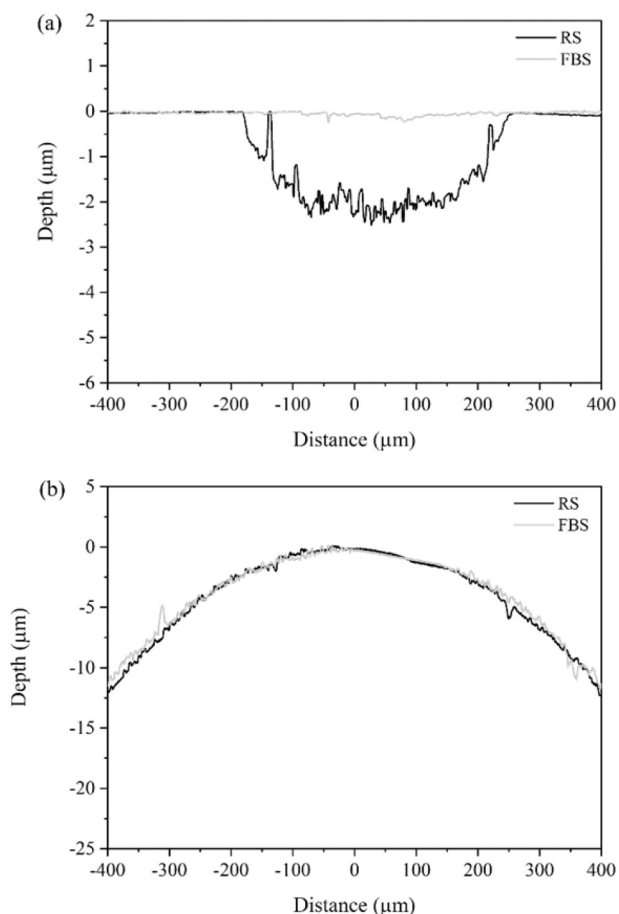
Fig. 16. 2D scar profiles for the coated CrN/S CoCrMo (a) discs and (b) counterfaces after tribocorrosion testing for 24 h in Ringer's solution and diluted FBS.

in the presence of proteins, compared to testing in the absence of proteins, was also observed by Muñoz and Gil [36] and Taufiqurrakhman et al. [37] when conducting tribocorrosion tests on a CoCrMo alloy against an alumina counterface. The authors [36,37] explained that a

three-body abrasive situation was established within the contact by the presence of debris particles entrapped between the disc and counterface. In the presence of protein, the debris aggregates with the protein molecules to form large particles such that the amount of mechanical wear is increased. In this work, a higher amount of agglomerated debris was visibly adhered to the sides of the uncoated ball scar following tests in FBS and despite the extent of mechanical material loss amount was similar to tests in Ringer's solution, an enhanced third body damage in the presence of proteins would not be excluded.

The CrN/S tribopair displayed a ~28 times reduction in material loss volume compared to the uncoated tribopair in Ringer's solution (Fig. 10). The CrN/S tribopair displayed low volume losses (Fig. 10) and a low coefficient of friction in both electrolytes (Figs. 4b and 7b). The wear-enhanced corrosion losses did not change much upon changing the electrolyte (dynamic current <1 µA in Figs. 4a and 7a) while the mechanical wear component decreased even further to become almost negligible in FBS. This resulted in the $\frac{C^*}{W^*}$ ratio to change significantly from 0.9 in Ringer's to >10 in FBS (Fig. 10). However, it is to be noted that both components of material loss were very small and therefore a small change in any of the loss components will greatly alter the $\frac{C^*}{W^*}$ ratio. This response was largely expected because the topmost CrN layer is known to be inherently resistant against Type I corrosion-wear [17,19,22]. As shown by the schematic presented in Fig. 18a, while testing in Ringer's solution resulted in a smooth removal of the top CrN layer (Fig. 5c, d), testing in FBS resulted in negligible damage of the CrN layer (Fig. 8c, d). Moreover, when testing in diluted FBS, the friction trace suggests that, similar to the uncoated tribopair, a lubricating film has formed on the tribopair surfaces (Fig. 18a). Whereas the COF for tests in Ringer's solution exhibited an initial region where the COF decreased with sliding time (Fig. 4b), such region was absent for tests in diluted FBS (Fig. 7b). Nonetheless, this layer has resulted in further reduction in volume loss (Fig. 10) and rendering the disc scar featureless, unlike the scar produced in Ringer's solution which contains minor grooves aligned in the sliding direction. Despite attaining lower volumetric losses in diluted FBS for CrN/S, the corrosion-wear mechanism remained largely unchanged when changing the electrolyte from Ringer's solution to FBS (Fig. 18a). This is evidence of the inherent ability of the hard ceramic coating against Type I corrosion-wear damage. Furthermore, Type II corrosion-wear [22] was non-existent since no evidence of blistering-type damage on the coated materials could be observed in the scars and the measured anodic current was very small
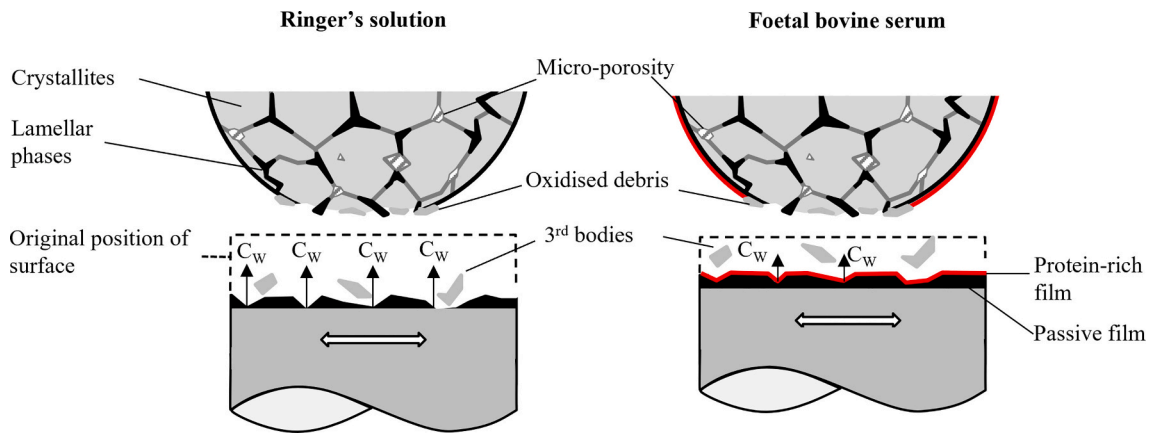
Fig. 17. Proposed tribocorrosion mechanism following sliding of the uncoated tribopairs under AP conditions in both Ringer's solution and diluted FBS.
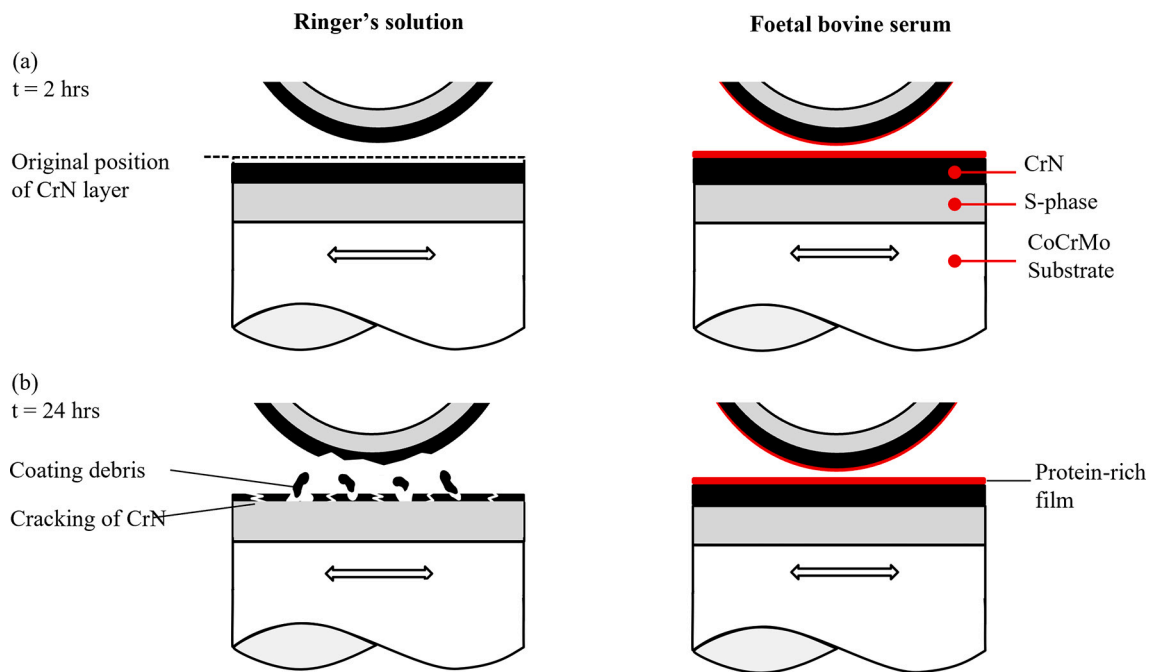

Fig. 18. Proposed tribocorrosion mechanism for the coated CrN/S tribopairs under AP conditions in both Ringer's solution and diluted FBS following (a) 2 h, and (b) 24 h of sliding.

following the cessation of sliding.

For longer duration tests, extensive grooving marks resulted within the scars of both the CrN/S disc (Fig. 13a) and CrN/S ball (Fig. 13b) following testing in Ringer's solution – such grooving marks were not present following the 2 h sliding tests where the outer CrN coating layer remained intact. For the 24-h tests in Ringer's solution, CrN coating micro-cracking and delamination on the disc produced a source for coating debris (Fig. 18b). Such debris was entrained within the contact zone during tribocorrosion testing resulting in three-body micro-abrasion damage (Fig. 13a, b). The microcracks forming inside the corrosion-wear track (Fig. 14a) were shown, using FIB analysis, to propagate within the outer coating layer but did not form or propagate in the tougher underlying S-phase layer (Fig. 15b).

Scar profiles following tests in Ringer's solution on regions exhibiting micro-cracking of the outer CrN layer (Fig. 16a) revealed that the maximum scar depth was approaching perforation of the CrN layer. It is possible that the presence of sufficient amount of debris resulting from polishing wear within the contact zone resulted in localised high contact stresses. Sufficiently high shear stresses were generated to cause local

yielding of the remaining very thin CrN layer causing the latter to collapse - a process commonly referred to as Hertzian failure or thin-ice-effect [19]. The ensuing local detachment of the outer CrN layer resulted in further hard CrN debris generation which, in addition to three-body abrasion damage, promoted progressive damage of the still intact CrN layer (Fig. 13a, b). Ways to mitigate this failure mechanism need to be further explored due to the possibility that in the real application high localised stresses may be encountered such as in the presence of hard fragments in the articulating surface or malalignment of the bearing surfaces. Hard coating failure can result in much higher material loss rates as reported by Leslie et al. [24] for MoM implants operating under adverse conditions.

In the present study, no coating damage was observed in FBS following both 2 h and 24 h of sliding where the extent of material loss was very small showing that the coating could withstand many cycles of stresses. These results are in agreement with hip simulator studies by Fisher et al. [38] and Leslie et al. [23] who reported lower material losses on CrN-coated CoCrMo tribopairs when compared to uncoated ASTM F75-18 CoCrMo tribopairs. The authors [23,38] concur that the

PVD CrN coatings are exceptional candidates for bearing surfaces due to the ultra-low wear they produced along with the barrier they provided to the release of Co ions.

From the results, it is apparent that the dual-layered CrN/S coating considerably improved the tribocorrosion performance of the uncoated CoCrMo tribopair in both test electrolytes. The beneficial attributes of the CrN/S coating include its low COF and the low mechanical and chemical tribocorrosion losses. Furthermore, nano-scratch results (Fig. 3c, d) have shown that the coating displayed good resistance to damage during scratch testing. The coated tribopair exhibited very good tribocorrosion performance in FBS. Tests in FBS of a longer duration shall be considered to assess the susceptibility to cracking and delamination of the CrN. Such long-term testing will give a better insight of whether the outer CrN layer will be consumed gradually or exhibit catastrophic cracking and delamination.

5. Limitations & future work

A limitation of this study is the assumption of the valence state for the oxidation of metallic transitional elements in the calculation of the oxidation losses using Faraday's Law. Another limitation is that the benchtop tests presented in this study do not replicate the biomechanics of a MoM hip joint but have as their main intention the ranking of potential biomaterials and coatings.

In this work, elastic contact stresses higher than those commonly experienced under standard walking conditions [27] were employed. However, it will be of scientific and industrial importance to also investigate higher contact stresses that will result in plastic contact conditions. Corrosion and tribocorrosion investigation of pre-damaged coated CoCrMo to simulate scenarios where the coating is damaged during surgery or during its implanted lifetime, would also be of interest.

6. Conclusions

High hardness (~20.1 GPa) scratch resistant dual layered coatings (CrN on carbon-rich CoCrMo S-phase termed CrN/S) have been magnetron sputter deposited onto wrought low-carbon (<0.2 wt%) biomedical grade CoCrMo alloy (ASTM F1537-20) test discs and CoCrMo alloy (Stellite® 21) balls to assess degradation rates under tribocorrosion test conditions that approach those found on metal-on-metal and a hypothetical coated-on-coated bearing surface combinations intended for use in human joint replacement devices like total hip replacements. The effect of test electrolyte (lubricant) composition, one based on Ringer's solution and the other based on foetal bovine serum (FBS), used at a temperature of 37 ± 1 °C was also investigated. The main findings, when using a normal test load of 3 N, corresponding to a maximum contact pressure of 630 MPa, were:

1. The dynamic COF of the uncoated tribopairs decreased from ~0.6 in Ringer's solution to ~0.15 in FBS, suggesting the formation of a lubricious protein-rich layer on the surface.
2. The dual layered CrN/S coating mitigated against mechanical and chemical damage (>95% reduction in total volume losses). The coated tribopair exhibited a smooth scar morphology synonymous with polishing wear in both test solutions following 2 h of sliding.
3. Testing for 24 h in Ringer's solution resulted in micro-cracking and delamination of the outer CrN layer due to local contact conditions resulting in very high contact stresses leading to the collapse of the CrN layer. The release of hard CrN debris triggered three-body abrasion damage, resulting in further coating delamination.
4. Long duration (24 h) testing in FBS only caused fine polishing of the coated bearing surfaces - no cracking or delamination took place.
5. Tribocorrosion losses were dominated by the formation and damage of the protective passive film (Type I corrosion-wear) of metal-on-metal bearings. Therefore, the use of inert coated-on-coated bearing surface combinations are likely to be significantly more durable (Type I corrosion-wear resistant) than conventional metal-on-metal bearing surfaces. Much longer duration testing of coated-on-coated bearing surface combinations are therefore justified.

CRediT authorship contribution statement

Antonino Mazzonello: Methodology, Formal analysis, Investigation, Data curation, Writing – original draft, Visualisation, Funding acquisition. **Joseph Buhagiar:** Methodology, Resources, Writing – review & editing, Supervision, Project administration, Funding Acquisition. **Raisa Chetcuti:** Methodology, Investigation, Data curation, Writing – review & editing. **Peter A. Dearnley:** Methodology, Investigation, Resources, Writing – review & editing. **Andrea Valsesia:** Methodology, Investigation, Writing – review & editing. **Pascal Colpo:** Methodology, Resources, Writing – review & editing, Project administration. **Bertram Mallia:** Conceptualisation, Methodology, Resources, Writing – review & editing, Supervision, Project administration, Funding acquisition.

Declaration of competing interest

The authors declare that they have no known competing financial interests or personal relationships that could have appeared to influence the work reported in this paper.

References

[1] J. Rituerto Sin, X. Hu, N. Emami, Tribology, corrosion and tribocorrosion of metal on metal implants, Tribol. - Mater. Surf. Interfaces 7 (2013) 1–12.
[2] W.Q. Toh, X. Tan, A. Bhowmik, E. Liu, S.B. Tor, Tribochemical characterization and tribocorrosive behavior of CoCrMo alloys: a review, Materials 11 (2018) 1–21.
[3] A.J. Smith, P. Dieppe, K. Vernon, M. Porter, A.W. Blom, Failure rates of stemmed metal-on-metal hip replacements: analysis of data from the National Joint Registry of England and Wales, Lancet 379 (2012) 1199–1204.
[4] J. Drummond, P. Tran, C. Fary, Metal-on-metal hip arthroplasty: a review of adverse reactions and patient management, J. Funct. Biomater. 6 (2015) 486–499.
[5] Q. Chen, G.A. Thouas, Metallic implant biomaterials, Mater. Sci. Eng. R. Rep. 87 (2015) 1–57.
[6] D. Dowson, C. Hardaker, M. Flett, G.H. Isaac, A hip joint simulator study of the performance of metal-on-metal joints: part I: the role of materials, J. Arthroplast. 19 (2004) 118–123.
[7] M.T. Mathew, M.A. Wimmer, Tribocorrosion in artificial joints: *in vitro* testing and clinical implications, in: D. Landolt, S. Mischler (Eds.), Tribocorrosion of Passive Metals and Coatings, Woodhead Publishing Limited, 2011, pp. 368–400.
[8] Department of Health and Human Services Food and Drug Administration, Effective date of requirement for premarket approval for total metal-on metal semi-constrained hip joint systems, Fed. Regist. 81 (2016) 8146–8149.
[9] Food and Drug Administration, Metal-on-metal Hip Implants. https://www.fda.gov/medical-devices/implants-and-prosthetics/metal-metal-hip-implants, 2019. (Accessed 9 February 2022).
[10] H.C. Amstutz, M.J. Le Duff, Hip resurfacing: history, current status, and future, Hip Int. 25 (2015) 330–338.
[11] S.R. Knight, R. Aujla, S.P. Biswas, Total Hip Arthroplasty-over 100 years of operative history, Orthop. Rev. 3 (2011).
[12] Y. Sun, P.A. Dearnley, Tribocorrosion behavior of duplex S/Cr (N) and S/Cr (C) coatings on CoCrMo alloy in 0.89% NaCl solution, J. Bio- Tribo-Corros. 1 (2015) 1–13.
[13] G. Zhang, P. Yan, P. Wang, Y. Chen, J. Zhang, Influence of nitrogen content on the structural, electrical and mechanical properties of CrNx thin films, Mater. Sci. Eng. A 460 (2007) 301–305.

[14] S. Lei, Y.R. Zhang, Y.X. Wang, J.L. Li, X. Jiang, J.M. Chen, Corrosion and wear behaviors of PVD CrN and CrSiN coatings in seawater, Trans. Nonferrous Metals Soc. China 26 (2016) 175–184.

[15] P. Perillo, Properties of CrN coating prepared by physical vapour deposition, Am. J. Mater. Sci. Applic. 3 (2015) 38–43.

[16] F. Cai, Q. Yang, X. Huang, R. Wei, Microstructure and corrosion behavior of CrN and CrSiCN coatings, J. Mater. Eng. Perform. 19 (2010) 721–727.

[17] R. Chetcuti, P.A. Dearnley, A. Mazzonello, J. Buhagiar, B. Mallia, Tribocorrosion response of duplex layered CoCrMoC/CrN and CrN/CoCrMoC coatings on implant grade 316LVM stainless steel, Surf. Coat. Technol. 384 (2020) 1–13.

[18] J. Buhagiar, H. Dong, Corrosion properties of S-phase layers formed on medical grade austenitic stainless steel, J. Mater. Sci. Mater. Med. 23 (2012) 271–281.

[19] P.A. Dearnley. Introduction to Surface Engineering, Cambridge University Press, New York, 2017.

[20] D. Formosa, R. Hunger, A. Spiteri, H. Dong, E. Sinagra, J. Buhagiar, Corrosion behaviour of carbon S-phase created on Ni-free biomedical stainless steel, Surf. Coat. Technol. 206 (2012) 3479–3487.

[21] J. Cassar, B. Mallia, A. Mazzonello, A. Karl, J. Buhagiar, Improved tribocorrosion resistance of a CoCrMo implant material by carburising, Lubricants 6 (2018) 1–18.

[22] P.A. Dearnley, G. Aldrich-Smith, Corrosion–wear mechanisms of hard coated austenitic 316L stainless steels, Wear 256 (2004) 491–499.

[23] I.J. Leslie, S. Williams, C. Brown, J. Anderson, G. Isaac, P. Hatto, E. Ingham, J. Fisher, Surface engineering: a low wearing solution for metal-on-metal hip surface replacements, J. Biomed. Mater. Res. Part B Appl. Biomater. 90 (2009) 558–565.

[24] I. Leslie, S. Williams, G. Isaac, P. Hatto, E. Ingham, J. Fisher, Wear of surface-engineered metal-on-metal bearings for hip prostheses under adverse conditions with the head loading on the rim of the cup, Proc. Inst. Mech. Eng. H 227 (2013) 345–349.

[25] D. Mazzucco, R. Scott, M. Spector, Composition of joint fluid in patients undergoing total knee replacement and revision arthroplasty: correlation with flow properties, Biomaterials 25 (2004) 4433–4445.

[26] J. Cassar, B. Mallia, A. Karl, J. Buhagiar, The effect of sliding onto the metal-electrolyte interface: studying model parameter modifications by means of EIS, Mater. Sci. Eng. C 75 (2017) 1366–1375.

[27] F. Liu, S. Williams, J. Fisher, Effect of microseparation on contact mechanics in metal-on-metal hip replacements—a finite element analysis, J. Biomed. Mater. Res. B Appl. Biomater. 103 (2015) 1312–1319.

[28] J. Williams, Engineering Tribology, Cambridge University Press, 2005.

[29] F.C. Caiazzo, V. Sisti, S.P. Trasatti, S. Trasatti, Electrochemical characterization of multilayer Cr/CrN-based coatings, Coatings 4 (2014) 508–526.

[30] K. Sadiq, M. Stack, R.A. Black, Wear mapping of CoCrMo alloy in simulated bio-tribocorrosion conditions of a hip prosthesis bearing in calf serum solution, Mater. Sci. Eng. C 49 (2015) 452–462.

[31] J. Perret, E. Boehm-Courjault, M. Cantoni, S. Mischler, A. Beaudouin, W. Chitty, J.-P. Vernot, EBSD, SEM and FIB characterisation of subsurface deformation during tribocorrosion of stainless steel in sulphuric acid, Wear 269 (2010) 383–393.

[32] M. Wimmer, M. Laurent, M. Mathew, C. Nagelli, Y. Liao, L. Marks, J. Jacobs, A. Fischer, The effect of contact load on CoCrMo wear and the formation and retention of tribofilms, Wear 332 (2015) 643–649.

[33] Y. Liao, E. Hoffman, M. Wimmer, A. Fischer, J. Jacobs, L. Marks, CoCrMo metal-on-metal hip replacements, Phys. Chem. Chem. Phys. 15 (2013) 746–756.

[34] Y. Yan, A. Neville, D. Dowson, Biotribocorrosion—an appraisal of the time dependence of wear and corrosion interactions: II. Surface analysis, J. Phys. D. Appl. Phys. 39 (2006) 3206–3212.

[35] Y. Yan, A. Neville, D. Dowson, Biotribocorrosion of CoCrMo orthopaedic implant materials—assessing the formation and effect of the biofilm, Tribol. Int. 40 (2007) 1492–1499.

[36] R.A. Gil, A.I. Muñoz, Influence of the sliding velocity and the applied potential on the corrosion and wear behavior of HC CoCrMo biomedical alloy in simulated body fluids, J. Mech. Behav. Biomed. Mater. 4 (2011) 2090–2102.

[37] M. Taufiqurrakhman, M.G. Bryant, A. Neville, Tribofilms on CoCrMo alloys: understanding the role of the lubricant, Biotribology 19 (2019) 1–10.

[38] J. Fisher, X. Hu, T. Stewart, S. Williams, J. Tipper, E. Ingham, C. Davies, P. Hatto, J. Bolton, Wear of surface engineered metal-on-metal hip prostheses, J. Mater. Sci. Mater. Med. 15 (2004) 225–235.